

AD-A278 568



PL-TR-93-2260

(2)

**AN INVESTIGATION OF METHODS FOR
IMPROVING MODELS OF IONOSPHERIC
PLASMA-DENSITY IRREGULARITIES
AND RADIO-FREQUENCY SCINTILLATION**

James A. Secan
Robert M. Bussey

DTIC
ELECTE
MAR 28 1994
S F D

Northwest Research Associates, Inc.
P.O. Box 3027
Bellevue, WA 98009-3027

1 November 1993

55A
94-09446



Scientific Report No. 2

Approved for public release; distribution unlimited



**PHILLIPS LABORATORY
Directorate of Geophysics
AIR FORCE MATERIEL COMMAND
HANSOM AIR FORCE BASE, MA 01731-3010**

94 3 25 002

"This technical report has been reviewed and is approved for publication"

Santimay Basu
(Signature)
SANTIMAY BASU
Contract Manager

Edward J. Berghorn
(Signature)
EDWARD J. BERGHORN, Major, USAF
Branch Chief

William K. Vickery
(Signature)
WILLIAM K. VICKERY
Division Director

This report has been reviewed by the ESC Public Affairs Office (PA) and is releasable to the National Technical Information Service (NTIS).

Qualified requestors may obtain additional copies from the Defense Technical Information Center (DTIC). All others should apply to the National Technical Information (NTIS).

If your address has changed, if you wish to be removed from the mailing list, or if the addressee is no longer employed by your organization, please notify PL/TSI, 29 Randolph Road, Hanscom AFB, MA 01731-3010. This will assist us in maintaining a current mailing list.

Do not return copies of this report unless contractual obligations or notices on a specific document require that it be returned.

REPORT DOCUMENTATION PAGE

Form Approved
OMB No. 0704-0788

Public reporting burden for this collection of information is estimated to average 1 hour per response, including the time for reviewing instructions, searching existing data sources, gathering and maintaining the data needed, and completing and reviewing the collection of information. Send comments regarding this burden estimate or any other aspect of this collection of information, including suggestions for reducing this burden, to Washington Headquarters Services, Directorate for Information Operations and Reports, 1215 Jefferson Davis Highway, Suite 1204, Arlington, VA 22202-4302, and to the Office of Management and Budget, Paperwork Reduction Project (0704-0188), Washington, DC 20503.

1. AGENCY USE ONLY (Leave blank)	2. REPORT DATE	3. REPORT TYPE AND DATES COVERED
	1 November 1993	Scientific No. 2
4. TITLE AND SUBTITLE An Investigation of Methods for Improving Models of Ionospheric Plasma-Density Irregularities and Radio-Frequency Scintillation		5. FUNDING NUMBERS F19628-91-C-0152 PE63707F PR AWS9 TA 10 WU AA
6. AUTHOR(S) James A. Secan, Robert M. Bussey		
7. PERFORMING ORGANIZATION NAME(S) AND ADDRESS(ES) Northwest Research Associates, Inc. P.O. Box 3027 Bellevue, WA 98009-3027		8. PERFORMING ORGANIZATION REPORT NUMBER NWRA-CR-93-R104
9. SPONSORING/MONITORING AGENCY NAME(S) AND ADDRESS(ES) Phillips Laboratory 29 Randolph Road Hanscom AFB, MA 01731-3010 Contract Manager: Santimay Basu/GPTA		10. SPONSORING/MONITORING AGENCY REPORT NUMBER PL-TR-93-2260
11. SUPPLEMENTARY NOTES The model development will benefit AF Space Forecast Center to support customers		
12a. DISTRIBUTION/AVAILABILITY STATEMENT approved for public release; distribution unlimited		12b. DISTRIBUTION CODE
13. ABSTRACT (Maximum 200 words) Many modern military systems used for communications, command and control, navigation, and surveillance depend on reliable and relatively noise-free transmission of radiowave signals through the earth's ionosphere. Small-scale irregularities in the ionospheric density can cause severe distortion, known as radiowave scintillation, of both the amplitude and phase of these signals. The WBMOD computer program can be used to estimate these effects on a wide range of systems. The objective of this study is to investigate improvements to the WBMOD model based on extensive data sets covering both the equatorial and high-latitude regimes. This report summarizes the work completed during the second year, which includes completion of the new models for the equatorial region and initial development of the models for the high latitude (auroral and polar cap) region.		
14. SUBJECT TERMS ionosphere, ionospheric density irregularities, equatorial region radiowave scintillation, modelling		15. NUMBER OF PAGES 58
		16. PRICE CODE
17. SECURITY CLASSIFICATION OF REPORT Unclassified	18. SECURITY CLASSIFICATION OF THIS PAGE Unclassified	19. SECURITY CLASSIFICATION OF ABSTRACT Unclassified
		20. LIMITATION OF ABSTRACT SAR

NSN 7540-01-280-5500

Standard Form 298 (Rev. 2-89)
Prescribed by ANSI Std. Z39-18
290-192

CONTENTS

	Page
Preface	vii
1. Introduction	1
2. Equatorial Model Development	1
2.1 Solar Cycle Variation	1
2.2 Geomagnetic Activity Variation	6
2.3 Diurnal Variation	9
2.4 Seasonal Variation	12
2.5 WBMOD Version 12	13
3. High Latitude Model Development	14
3.1 Model Plan	14
3.2 $C_k L$ Calculation	15
3.3 Preliminary Results	16
4. Conclusion	23
References	23
Appendix A. Data Plots — Variation with Solar Cycle	25
Appendix B. Data Plots — Variation with Geomagnetic Activity (K_p)	35
Appendix C. Data Plots — Variation with Geomagnetic Activity (K_{pSS})	43

Accession For	
NTIS	CRA&I
DTIC	TAB
Unannounced	
Justification	
By	
Distribution /	
Availability Codes	
Dist	Avail and / or Special
A-1	

Illustrations

- 1 Distribution functions of $\log(C_k L)$ calculated from the Ancon and Kwajalein data sets. The $\log(C_k L)$ values were calculated from the VHF σ_ϕ observations, and only data from the night passes were included. Three distributions are plotted, one for each of three SSN ranges: $SSN \leq 50$, $50 < SSN \leq 100$, and $SSN > 100$. 2
- 2 Scatter plot of $\log(C_k L)$ calculated from the Ancon and Kwajalein data sets. The $\log(C_k L)$ values were calculated from the VHF σ_ϕ observations, and only data from the night passes were included. 2
- 3 Variation of $Pr_{S4}(0.5)$ as a function of SSN at Ascension Island (L-band), Manila (VHF), and Huancayo (VHF). The data used were limited to low geomagnetic activity, post-sunset, and near-equinox (see text for details). 4
- 4 The variation of $Pr_{S4}(0.5)$ as a function of K_{pSS} at Ascension Island (L-band), Manila (VHF), and Huancayo (VHF). The data used were limited to post-sunset and near-equinox (see text for details). 8
- 5 Variation of $SI(dB)$ as a function of time for four levels of geomagnetic activity taken from the model of Aarons [1985]. 9
- 6 Variation of $SI(dB)$ as a function of day of the year for four levels of geomagnetic activity taken from the model of Aarons [1985]. 10
- 7 Bin-averaged behavior of $\log(C_k L)$ at Bellevue as a function of the distance in geomagnetic latitude from the high-latitude precipitation boundary and geomagnetic local time. The boundary location was derived from the DMSP SSJ boundary database. 18
- 8 Bin-averaged behavior of $\log(C_k L)$ at Poker Flat as a function of the distance in geomagnetic latitude from the high-latitude precipitation boundary and geomagnetic local time. The boundary location was derived from the K_p -dependent model described in the text. 19
- 9 Bin-averaged behavior of $\log(C_k L)$ at Tromso as a function of the distance in geomagnetic latitude from the high-latitude precipitation boundary and geomagnetic local time. The boundary location was derived from the DMSP SSJ boundary database. 20
- 10 Bin-averaged behavior of $\log(C_k L)$ at Ft. Churchill as a function of the distance in geomagnetic latitude from the high-latitude precipitation boundary and geomagnetic local time. The boundary location was derived from the DMSP SSJ boundary database. 21

11 Bin-averaged behavior of $\log(C_k L)$ at Sondre Stromfjord as a function of 22
 the distance in geomagnetic latitude from the high- latitude precipitation
 boundary and geomagnetic local time. The boundary location was derived
 from the DMSP SSJ boundary database.

Tables

1 SSN variation constants for the equatorial and anomaly-crest μ models. 3
 2 Number of data points as a function of SSN. The three numbers in each cell 5
 are the total number of observations (top), the number of observations of
 $S_4 > 0.5$ (middle), and the percent of time that S_4 exceeded 0.5 (bottom).
 3 Values for η_{00} and η_s in the equatorial and anomaly-crest models. 6
 4 Number of data points as a function of K_p . The three numbers in each cell 7
 are the total number of observations (top), the number of observations of
 $S_4 > 0.5$ (middle), and the percent of time that S_4 exceeded 0.5 (bottom).
 5 Number of data points as a function of K_{pSS} . The three numbers in each 7
 cell are the total number of observations (top), the number of observa-
 tions of $S_4 > 0.5$ (middle), and the percent of time that S_4 exceeded 0.5
 (bottom).
 6 Values for the constants in the diurnal variation for the equatorial and 12
 anomaly-crest models.
 7 Values for the constants in the $W_{s,high}$ equation for the equatorial and 13
 anomaly-crest models.
 8 Data available for use in the high-latitude model upgrade. 15

PREFACE

This report summarizes the work completed during the second year of a project focused on improving the WBMOD model of ionospheric scintillation. This work is part of a larger effort which has the overall objective of providing the USAF Air Weather Service with an improved capability for providing support to their customers who are impacted by ionospheric scintillation effects.

We would like to thank Dr. Santimay Basu of the USAF Phillips Laboratory (PL/GPIA) for his guidance and suggestions for improving the model, and Dr. Fred Rich (PL/GPSG) for providing the DMSP SSJ particle boundary data.

1. Introduction

Many modern military systems used for communications, command and control, navigation, and surveillance depend on reliable and relatively noise-free transmission of radiowave signals through the earth's ionosphere. Small-scale irregularities in the ionospheric density can cause severe distortion, known as radiowave scintillation, of both the amplitude and phase of these signals. A basic tool used in estimating these effects on systems is a computer program, WBMOD, based on a single-scatter phase-screen propagation model and a number of empirical models of the global morphology of ionospheric density irregularities. A recent validation of the WBMOD model showed that it was deficient in a number of areas. Much of this deficiency could be traced to the limited coverage of the data used in developing the model (a single station at high latitudes and two stations at equatorial latitudes). The objective of this study is to investigate and implement improvements to the WBMOD model based on more extensive data sets in both the equatorial and high-latitude regimes.

2. Equatorial Model Development

The development of the new equatorial model was completed during the report period, and the new model was implemented in version 12.00 of WBMOD. The work focused on completion of the variation of equatorial scintillation with *SSN* and with geomagnetic activity levels.

2.1. Solar Cycle Variation. Figure 1 shows the distribution of $\log(C_k L)$ calculated from VHF σ_s observations in the nighttime (near 2200 local time) Ancon and Kwajalein WIDEBAND data sets for three ranges of *SSN*, and Figure 2 is a scatter-plot of the same data as a function of *SSN*. A number of different behaviors can be noted in these plots:

1. The $\log(C_k L)$ values at the center of the peaks in the distribution (μ in the model PDF) increase with *SSN*. This behavior was noted in earlier modeling [Secan, 1989] and was included in previous version of WBMOD.
2. The width of the high-*SSN* peak ($\sigma_{2,night}$) decreases with increasing *SSN*.
3. The population in high-*SSN* peak ($\eta_{2,night}$) increases with *SSN*, but exhibits what appears to be a saturation effect at high *SSN*.

Since the other data sets were solely intensity data, they were not useful for determining the characteristics of the shape (σ) and location (μ) of the PDF peaks due to distortions at both ends of the distribution (noise-floor and data-reduction induced distortions at the lower end of the distribution, and saturation effects caused by Fresnel filtering at the higher end). We therefore decided to use the WIDEBAND phase-scintillation data shown in these figures to specify the *SSN* variation of these PDF parameters and to use the larger $SI(dB)$ -based data sets to specify the *SSN* variation of the parameter which determines the population in the "plume" peak, $\eta_{2,night}$. The $\sigma_{2,night}$ parameter varies linearly with *SSN* from 1.0 at

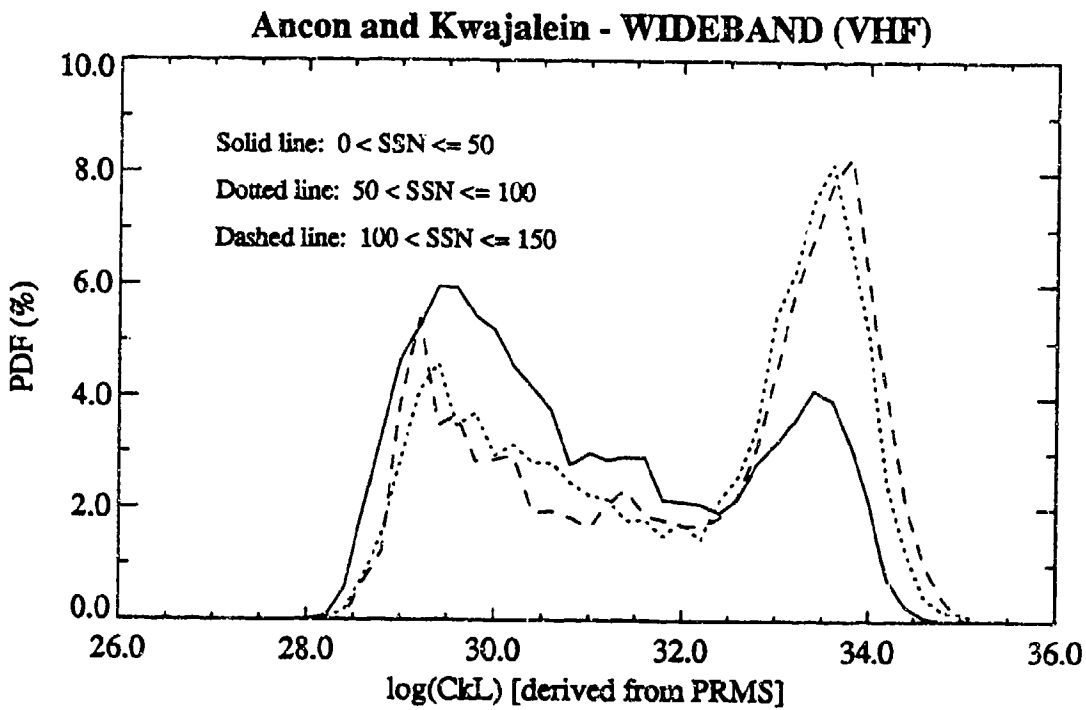


Figure 1: Distribution functions of $\log(C_k L)$ calculated from the Ancon and Kwajalein data sets. The $\log(C_k L)$ values were calculated from the VHF σ_ϕ observations, and only data from the night passes were included. Three distributions are plotted, one for each of three SSN ranges: $\text{SSN} \leq 50$, $50 < \text{SSN} \leq 100$, and $\text{SSN} > 100$.

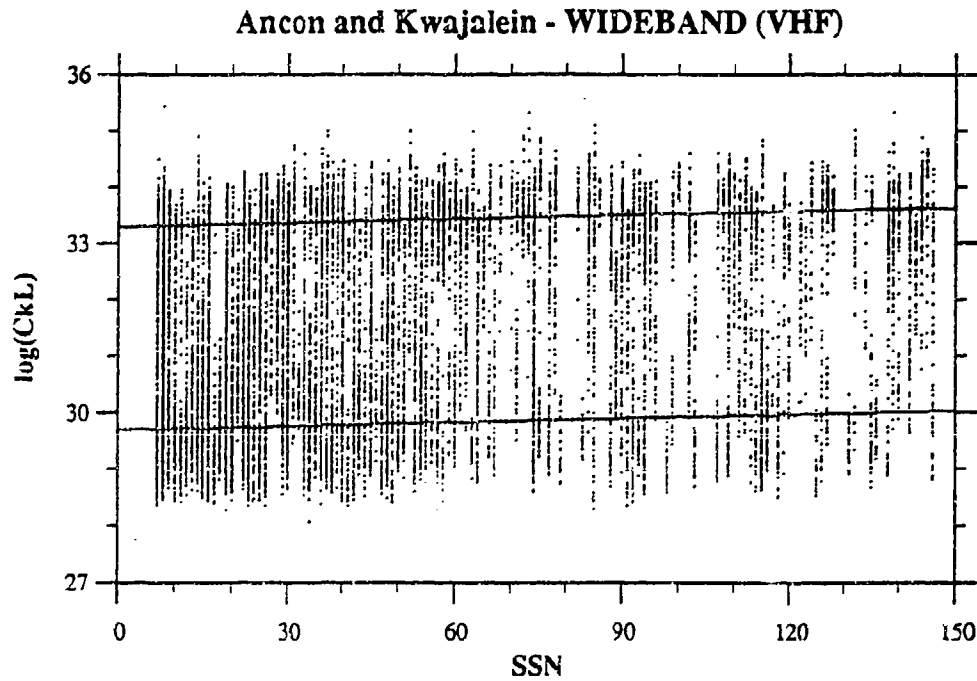


Figure 2: Scatter plot of $\log(C_k L)$ calculated from the Ancon and Kwajalein data sets. The $\log(C_k L)$ values were calculated from the VHF σ_ϕ observations, and only data from the night passes were included.

$SSN = 0$ to 0.8 at $SSN = SSN_s$, where SSN_s is the point at which the SSN variation "saturates" (this value is discussed later). The values of the four μ parameters also vary linearly with SSN . The constants of the linear equations, listed in Table 1, were extracted from the σ_ϕ -derived $\log(C_k L)$ data shown in Figure 2 and the corresponding daytime (near 1000 local time) data. Since there are no data of this type available for the anomaly crest region, the variations of $\sigma_{2,night}$ and three of the four μ parameters in the anomaly crest region are taken to be identical to that found in the WIDEBAND equatorial data. The only exception is the "DC" term in the variation of the $\log(C_k L)$ value for the plume peak — this was adjusted to agree with the levels of scintillation observed in the Ascension Island database as reported in Secan *et al.*, [1993a].

Parameter	Equatorial		Anomaly Crest	
	Intercept	Slope	Intercept	Slope
$\mu_{1,day}$	27.0	0.0022	27.0	0.0022
$\mu_{2,day}$	0.0	0.0	0.0	0.0
$\mu_{1,night}$	29.7	0.0002	29.7	0.0002
$\mu_{2,night}$	33.3	0.0022	35.8	0.0022

Table 1: SSN variation constants for the equatorial and anomaly-crest μ models.

The variation of the population in the plume peak (μ_2) of the PDF with SSN was modeled by matching the patterns of the diurnal/seasonal variation of the occurrence statistics for $S_4 > 0.5$ as seen in the $SI(dB)$ data sets. Appendix A contains the plots used in the modeling, and Table 2 summarizes the number of data points in each plot, the number of points for which S_4 exceeded 0.5, and the percent of time that S_4 exceeded 0.5. Figure 3 illustrates the variation of the $S_4 > 0.5$ occurrence statistic as a function of SSN . The data used in generating this figure were limited to low geomagnetic activity levels ($K_{pSS} \leq 20$, where K_{pSS} is the K_p value at local sunset), the first four hours after $t_e = 0$, and to the two sixty-day periods covering the periods of maximum scintillation activity for each station. [Note: Many of the plots in this report are of the occurrence statistic defined as the percent of the time that S_4 exceeds 0.5. This statistic will be denoted $Pr_{S4}(0.5)$ in the remainder of this report.]

In studying these plots, we have found the following behaviors:

1. $Pr_{S4}(0.5)$ increases with increasing SSN , with a tendency to reach "saturation" at a SSN value of 125 to 150.
2. The saturation levels for the two equatorial-VHF data sets are in fairly good agreement, but the level at Huancayo is significantly higher at low SSN than at Manila.

SSN Range	Ground Station		
	Ascension	Manila	Huancayo
All	34,262	31,181	56,746
	2,544	4,203	9,995
	7%	14%	18%
≤ 50	14,106	10,092	19,230
	59	476	1,949
	>1%	5%	10%
50 - 100	5,263	10,331	12,651
	407	1,068	1,825
	8%	10%	14%
100 - 150	8,615	7,422	13,185
	1,098	1,643	3,171
	13%	22%	24%
150 - 200	4,569	2,244	8,016
	706	609	2,103
	15%	27%	26%
> 200	1,709	1,092	3,664
	274	407	947
	16%	37%	26%
	L-band	VHF	VHF

Table 2: Number of data points as a function of SSN. The three numbers in each cell are the total number of observations (top), the number of observations of $S_4 > 0.5$ (middle), and the percent of time that S_4 exceeded 0.5 (bottom).

3. The ratio between the near-equinoctial maxima and the local-summer minimum reduces with increasing SSN.
4. The decay with time after the diurnal maximum decreases with increasing SSN at the equatorial stations, although not at Ascension Island.

These variations have been included in the model via the PDF parameter that describes the nighttime plume population, $\eta_{2,night}$, and the diurnal variation of the η_2 parameter.

The value for $\eta_{2,night}$ is calculated from

$$\eta_{2,night} = f_s(SSN, \phi_n) f_k(K_{pSS}) f_d(\phi_{term}) \quad (1)$$

where ϕ_n is a longitude parameter, K_{pSS} is the K_p valid at local sunset, and ϕ_{term} is the angle between the sunset terminator and the local geomagnetic meridian calculated at the

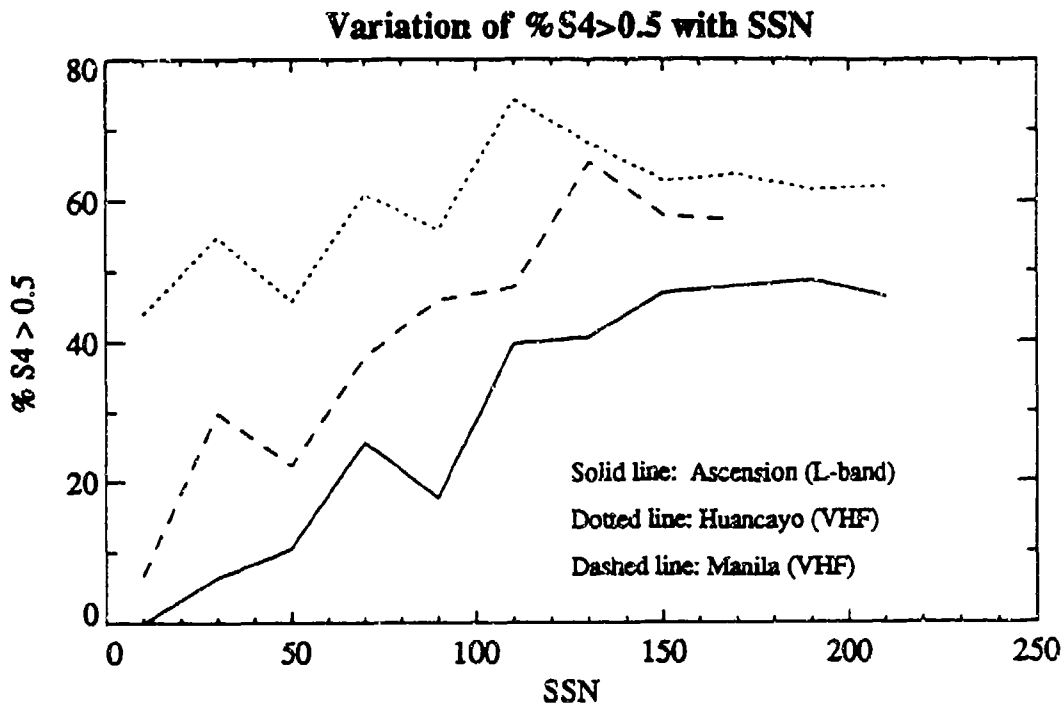


Figure 3: Variation of $Pr_{S4}(0.5)$ as a function of SSN at Ascension Island (L-band), Manila (VHF), and Huancayo (VHF). The data used were limited to low geomagnetic activity, post-sunset, and near-equinox (see text for details).

IPP. The three functions describe the variation of this parameter with SSN, K_{SS} (described in the next section), and season. The “zero” level is set in the f_s function, and the other two functions modulate this level.

The SSN variation shown by the data was a steady increase in $\eta_{2,night}$ with SSN, from a minimum value at $SSN = 0$ to a maximum at some “saturation” value of SSN, denoted SSN_s . The model transitions from the minimum value to the saturation value using a simple gaussian function of SSN as follows:

$$f_s = \eta_0 + (\eta_s - \eta_0) \exp \left[- \left(\frac{SSN' - SSN_s}{W_{ssn}} \right)^2 \right] \quad (2)$$

where η_0 and η_s are the minimum and saturation values for $\eta_{2,night}$, SSN' is the minimum of the observed SSN and the value of SSN_s , and W_{ssn} is calculated from other parameters so that f_s becomes arbitrarily close to the value of η_0 for $SSN' = 0$.

In fitting this modeled variation to the data, it became apparent that the SSN variation at Huancayo and Manila were impossible to reconcile without invoking a longitudinal difference between the two stations. This was included in the model by applying a longitudinal modulation on the η_0 parameter such that the value of this parameter in the vicinity of

Manila is a factor of 0.4 times the value in the Huancayo sector. The very non-uniform longitudinal coverage of the data set made it impossible to define this variation rigorously, so it has been implemented in the following simple form:

$$\eta_0 = [\eta_{lon} + (1 - \eta_{lon}) f_l(\phi)] \eta_{00} \quad (3)$$

where η_{lon} is 0.4 and f_l is given by

$$f_l(\phi) = 0.5 \left[\operatorname{erf} \left(\frac{\phi - \phi_1}{\Delta\phi} \right) - \operatorname{erf} \left(\frac{\phi - \phi_2}{\Delta\phi} \right) \right] \quad (4)$$

where ϕ is the geographic longitude; ϕ_1 and ϕ_2 are 60° and 210° , respectively and $\Delta\phi$ is set to 15° . These values were set in order to move the transitions away from the locations where we had data, and were based on review of the results documented in *Basu et al.* [1976] and *Maruyama and Matuura* [1984] from *in-situ* observations. [Note: This longitudinal variation replaces the one described in Scientific Report # 1 for this project (*Secan et al.* [1993a], denoted SR-1)].

The values for the constants η_s (in Equation [2]) and η_{00} (in Equation [3]) were extracted from the data sets, and are given in Table 3.

	Equatorial	Anomaly Crest
η_{00}	0.70	0.05
η_s	1.00	0.80

Table 3: Values for η_{00} and η_s in the equatorial and anomaly-crest models.

The models for the SSN component of the diurnal and seasonal variations are discussed in Sections 2.3 and 2.4, respectively.

2.2 Geomagnetic Activity Variation. As described in SR-1, we have decided to use the value of K_p at local sunset (denoted K_{pSS}) for modeling the variations in scintillation levels in the post-sunset period and the K_p value at the observation time for variations in the levels after the post-sunset peak in scintillation activity. Contour plots of the occurrence statistic $Pr_{S4}(0.5)$ similar to those generated for the SSN variation are provided in Appendix B as a function of K_p and in Appendix C as a function of K_{pSS} . The number of data points used to generate each figure, the number of points in each plot where $S_4 > 0.5$, and the percent of time that S_4 exceeded 0.5 are listed in Tables 4 (as a function of K_p) and 5 (as a function of K_{pSS}).

The steady decrease in the occurrence statistic evident in Table 5 can be seen clearly in Figure 4, which shows the variation of $Pr_{S4}(0.5)$ as a function of K_{pSS} from four of the

K_p Range	Ground Station		
	Ascension	Manila	Huancayo
All	75,613	80,155	124,474
	4,437	8,210	18,654
	6%	10%	15%
≤ 20	33,929	28,621	57,263
	2,407	3,335	8,395
	7%	12%	15%
$2+ - 40$	32,437	38,145	52,480
	1,690	3,758	7,699
	5%	10%	15%
$\geq 4+$	9,247	13,389	14,731
	340	1,117	2,560
	4%	8%	17%
	L-band	VHF	VHF

Table 4: Number of data points as a function of K_p . The three numbers in each cell are the total number of observations (top), the number of observations of $S_4 > 0.5$ (middle), and the percent of time that S_4 exceeded 0.5 (bottom).

K_{pSS} Range	Ground Station		
	Ascension	Manila	Huancayo
All	75,613	80,155	124,474
	4,437	8,210	18,654
	6%	10%	15%
≤ 20	4,262	31,181	56,746
	2,544	4,203	9,995
	7%	13%	18%
$2+ - 40$	31,743	37,415	51,679
	1,657	3,428	6,813
	5%	11%	13%
$\geq 4+$	9,608	11,559	16,049
	236	579	1,846
	2%	5%	12%
	L-band	VHF	VHF

Table 5 Number of data points as a function of K_{pSS} . The three numbers in each cell are the total number of observations (top), the number of observations of $S_4 > 0.5$ (middle), and the percent of time that S_4 exceeded 0.5 (bottom).

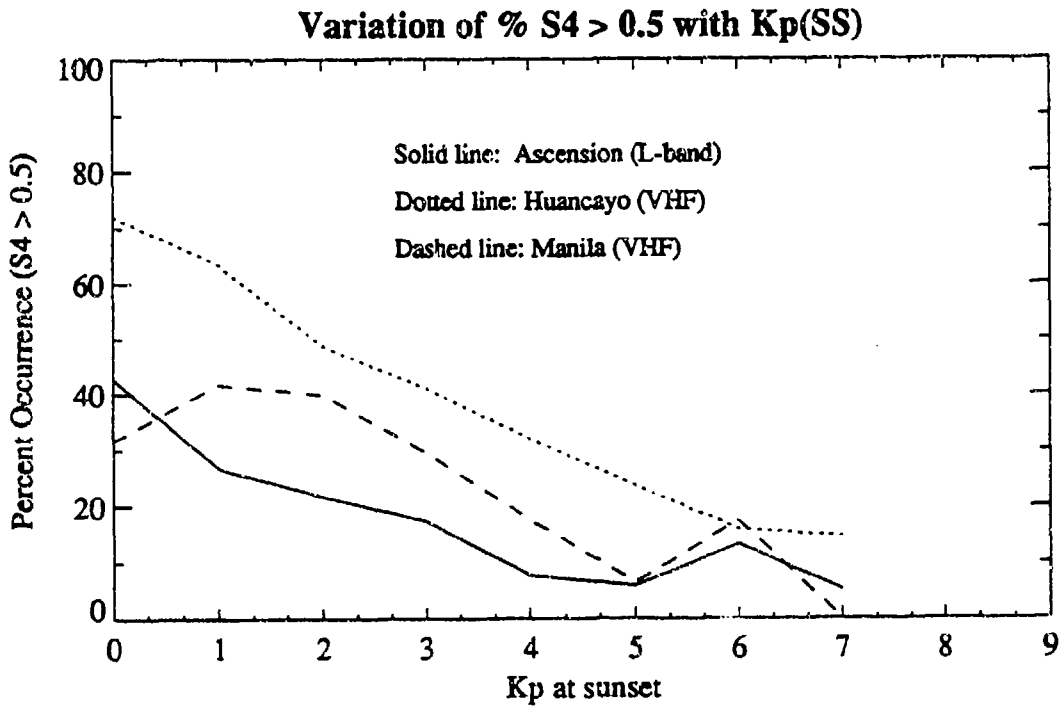


Figure 4: The variation of $Pr_{S4}(0.5)$ as a function of K_{pSS} at Ascension Island (L-band), Manila (VHF), and Huancayo (VHF). The data used were limited to post-sunset and near-equinox (see text for details).

data sets. The data used in generating this plot were limited to the first four hours after $t_c = 0$, and to the two sixty-day periods covering the periods of maximum scintillation activity for each station. With the exception of Manila, the data sets show a steady decrease in $Pr_{S4}(0.5)$ with K_{pSS} , with a tendency for the decrease to "level out" at a K_{pSS} value between 5° and 6° . *Aerons* [1985] included a similar decrease with increasing K_p in his model for the variation of $SI(dB)$ at Huancayo. Figure 5 shows the variation of $SI(dB)$ as a function of time for four values of K_p .

We have modeled this variation by varying the $\eta_{2,night}$ parameter as a function of K_{pSS} as follows:

$$f_k = 1.0 - 0.14K'_{pSS} \quad (5)$$

where K'_{pSS} is the minimum of the observed K_{pSS} and a value of 5.0. The value of 0.14 in Equation [5] fit both the Huancayo and Ascension Island data well, although the Manila data showed a slower drop with K_{pSS} for low activity levels.

In studying the various plots of changes in the diurnal/seasonal variation of $Pr_{S4}(0.5)$ with geomagnetic activity we have found the following:

1. The ratio of the scintillation level at the seasonal maxima (as measured by $Pr_{S4}(0.5)$) to

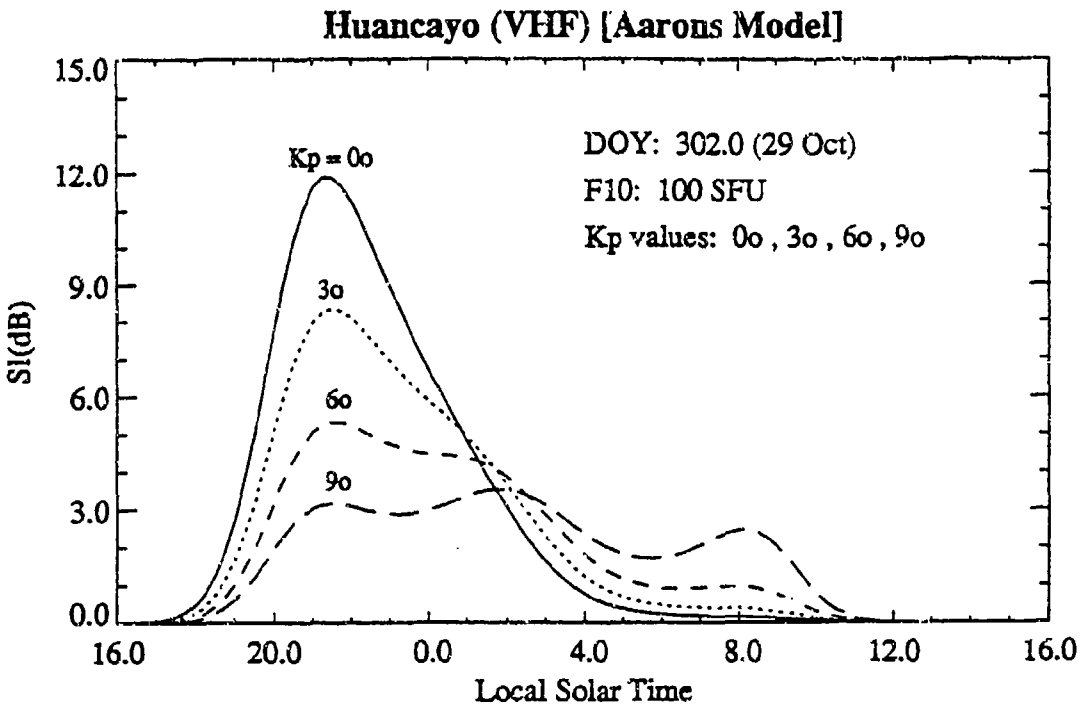


Figure 5: Variation of $SI(dB)$ as a function of time for four levels of geomagnetic activity taken from the model of *Aarons* [1985].

the level at the local summer minimum tends to decrease with increasing geomagnetic activity at the equatorial stations, but not at Ascension. This behavior was also included in the Aarons model, as can be seen in Figure 6.

2. As the level of geomagnetic activity increases, the value of $Pr_{s4}(0.5)$ increases in the late evening/early morning hours. This can also be seen in the Aarons model (see Figure 5).

These behaviors have been included in the diurnal and seasonal variation models described in the next two sections.

2.3 Diurnal Variation. The model of the diurnal variation described in SR-1 has been modified to include SSN and geomagnetic effects described in the previous two sections. The parameter that specifies the time after sunset at which the peak level of scintillation is reached, t_{ss} , has been modified to vary with SSN as follows:

$$t_{ss} = t_{ss,0} + \left(\frac{SSN'}{SSN_s} \right) t_{ss,ssn} \quad (6)$$

where SSN' and SSN_s are as defined in Section 2.1. The parameter which controls the rate at which the scintillation level decreases after the post-sunset maximum, W_{sr} , now varies

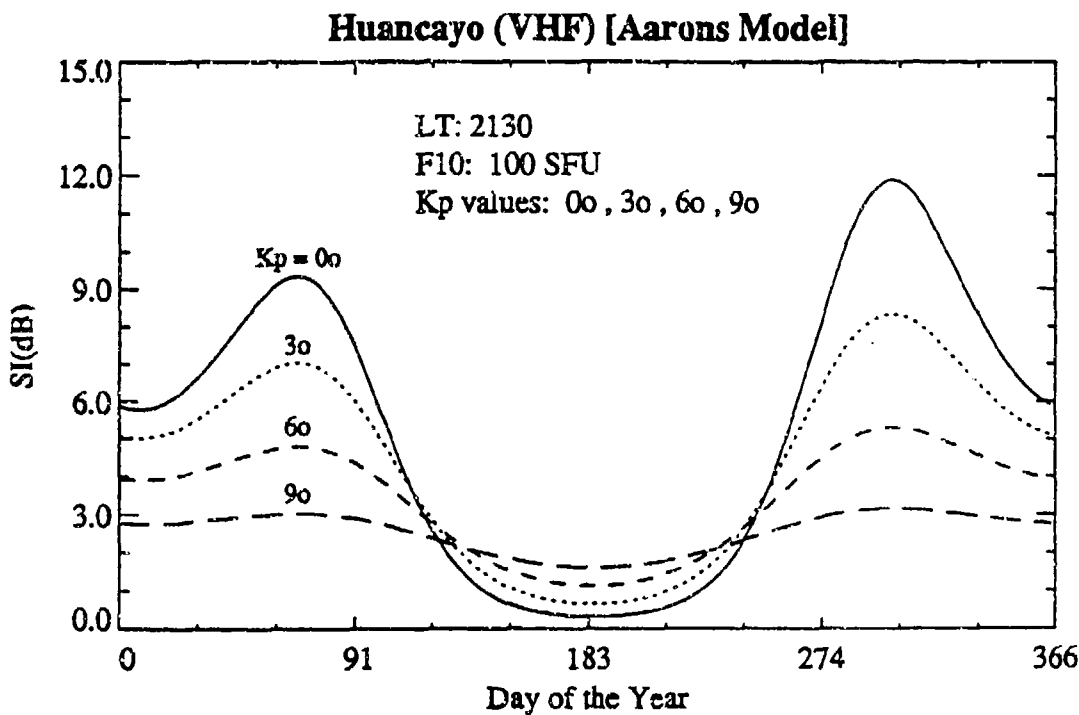


Figure 6: Variation of $SI(dB)$ as a function of day of the year for four levels of geomagnetic activity taken from the model of *Aarons* [1985].

with both SSN and K_p , as follows:

$$W_{sr} = W_{sr0} + \left(\frac{SSN'}{SSN_s} \right) W_{sr,ssn} + \left(\frac{\min(t_e, 10)}{C_0 + C_1 K'_p} \right) \quad (7)$$

where K'_p is the minimum of the observed K_p and a value of 5.0.

In a separate study, we found discontinuities in the diurnal variation of $\log(C_k L)$ in the new equatorial-region models. We have modified the way in which the diurnal variation is implemented in order to remove these discontinuities. These changes were as follows:

1. The function used to model the diurnal variation for the σ_i and η_i parameters (Equation

[6] in SR-1) was changed to

$$f(t_e) = \begin{cases} \exp \left[- \left(\frac{t_e - t_{ss}}{W_{ss}} \right)^2 \right] & \text{if } t_e < t_{ss} \\ 1.0 & \text{if } t_e \leq t_e \leq t_{sr} \\ \exp \left[- \left(\frac{t_e - t_{sr}}{W_{sr}} \right)^2 \right] & \text{if } t_{sr} < t_e \leq t_c \\ \exp \left[- \left(\frac{t_e - t_{sr}}{W_{sr}} \right)^2 \right] \exp \left[- \left(\frac{t_e - t_c}{W_c} \right)^2 \right] & \text{if } t_e > t_c \end{cases} \quad (8)$$

where t_e is the time past sunset, t_{ss} and W_{ss} are the peak time and half-width of the post-sunset gaussian, t_{sr} and W_{sr} are the time at which the late-evening/early-morning "sunrise" segment of the variation starts its decrease and the half-width in this segment, and t_c and W_c are the time at which the late-morning segment of the variation starts and the half-width in this segment.

2. The W_{ss} half-width is calculated from

$$W_{ss} = 0.466 t_{ss} \quad (9)$$

rather than a fixed value of 0.80^h .

3. The t_{sr} time is calculated from

$$t_{sr} = t_{ss} + 1.5^h \quad (10)$$

rather than a fixed value of 1.75^h .

4. The W_c half-width in Equation [8] is calculated from

$$W_c = 0.466 (t_0 - t_c) \quad (11)$$

5. The diurnal variation for the μ_i parameter has been altered so that the μ_1 (non-plume population) and μ_2 (plume population) parameters have slightly different variations. The new variations, which replace Equation [8] from SR-1, are

$$f_{\mu n-p}(t_e) = \begin{cases} f(t_e) & \text{if } t_e < t_{sr} \\ \left(\frac{t_e - t_c}{t_{sr} - t_c} \right) & \text{if } t_{sr} \leq t_e \leq t_0 \\ 0 & \text{if } t_e > t_0 \end{cases} \quad (12)$$

for the non-plume population, and

$$f_{\mu p}(t_e) = \begin{cases} 1.0 & \text{if } t_e \leq t_{sr} \\ f(t_e) & \text{if } t_e > t_{sr} \end{cases} \quad (13)$$

for the plume population.

These modifications do not change measurably the results presented in SR-1, as the discontinuities only appear for low scintillation levels ($S_4 < 0.1$) and low frequencies (< 100 MHz).

The model constants in Equations [6] and [13] are given in Table 6.

	Equatorial	Anomaly Crest
t_{ss0}	1.00	1.00
$t_{ss,ssn}$	0.50	0.20
t_c	10.00	10.00
t_0	16.00	16.00
W_{sr0}	0.50	1.50
$W_{sr,ssn}$	3.00	0.00
C_0	2.00	1.50
C_1	-0.06	-0.02

Table 6: Values for the constants in the diurnal variation for the equatorial and anomaly-crest models.

2.4 Seasonal Variation. The model for seasonal variation has been somewhat changed from the description in SR-1. The form of the variation has not changed, but the way in which the W_s parameter is calculated has. Rather than "summer" and "winter" values, the modeling for W_s is in terms of "high" and "low" values. These correspond to the values to be used in the solstice where the scintillation levels are either high (with respect to the levels at the other solstice) or low. The determination of which value for W_s is valid is a function of the season and of the longitude sector.

The "low" value for W_s , $W_{s,low}$, corresponds to what had been called the "winter" value, which has been changed to a fixed value of 13.0. The "high" value, $W_{s,high}$, corresponding to the old "summer" value, now varies with both SSN and K_{pSS} in order to replicate the seasonal behavior seen in the data. This parameter is now calculated from the following:

$$W_{s,high} = W_{s0} + W_{s,ssn}SSN' + W_{s,kp}K'_{pSS} \quad (14)$$

where the values for the three constants in this equation for the equatorial and anomaly-crest models are given in Table 7.

	Equatorial	Anomaly Crest
W_{s0}	16.0	16.0
$W_{s,ssn}$	-0.01	-0.01
$W_{s,kp}$	1.0	0.0

Table 7: Values for the constants in the $W_{s,high}$ equation for the equatorial and anomaly-crest models.

The selection of which of the two values to use for W_s is based on the season and on the longitude sector. In the Pacific sector (where $f_l = 1.0$ (see Equation [4])), $W_{s,high}$ is used on the June solstice side of the seasonal activity peaks and $W_{s,low}$ is used on the December solstice side. In the Atlantic sector ($f_l = 0.0$), $W_{s,low}$ is used on the June solstice side of the seasonal activity peaks and $W_{s,high}$ is used on the December solstice side. This is implemented in the model code as follows:

$$W_s = W_{s,low} - (W_{s,high} - W_{s,low}) f'_l(\phi) \quad (15)$$

where

$$f'_l(\phi) = \begin{cases} f_l(\phi) & \text{if } \phi_{term} \leq 0 \\ 1 - f_l(\phi) & \text{if } \phi_{term} > 0 \end{cases} \quad (16)$$

The rationale for this aspect of the model is the obvious difference in the solstitial behavior at the three Atlantic sector stations (Huancayo, Ancon, and Ascension Island) and that seen at the two Pacific sector stations (Manila and Kwajalein). This difference has been noted before (see *Basu et al.*, [1976] and *Maruyama and Matuura*, [1984]), and was included in a somewhat crude fashion in the last upgrade of the WBMOD equatorial model [*Secan*, 1989].

2.5 WBMOD Version 12. The new models for equatorial scintillation described in this report and SR-1 have been implemented in Version 12 of WBMOD. This version of WBMOD has the following changes from Version 11II:

1. The model for the irregularity strength parameter, $C_k L$, has been expanded from modeling merely the mean $C_k L$ value to modeling the full $\log(C_k L)$ PDF.
2. The equatorial model for $C_k L$ has been replaced.

3. The calculation of S_4 on a two-way path based on the theory developed by *Fremouw and Ishimaru* [1992] has been implemented. The user is requested to enter the correlation between the up- and down-links, a parameter which will be calculated by the model in a later implementation.
4. The user is given two options for model output: (1) the occurrence statistics for a user-specified level of scintillation, or (2) the level of scintillation for a user-specified occurrence percentile. The user may specify the scintillation level either in terms of S_4 or of σ_ϕ (if σ_ϕ is to be calculated).
5. The $SI(dB)$ intensity scintillation parameter is now calculated and included in the model output.

A User Guide was written for the research version of WBMOD. It presents a brief description of the model and describes how the model should be run [Secan, 1993]. Included in the User Guide are copies of papers presented at the 1987 and 1993 Ionospheric Effects Symposia [Secan et al., 1987; Secan et al., 1993b] to augment the model description. Copies of this document were provided to PL/GPIA and to the Air Force Space Forecast Center (AFSFC). The AFSFC also received a copy of the research version of WBMOD 12.02 compiled to run on an Intel 80386-class computer.

3. High-Latitude Model Development

With completion of the equatorial region of the model, attention has been moved to upgrading the high-latitude region. A very different set of data will be used in this part of the model-upgrade effort from that used in the equatorial upgrade. As with the equatorial database, one of the components of the high-latitude database is a set of data taken from the WIDEBAND satellite experiment, collected at Poker Flat, Alaska. The remaining data were collected from the HiLat and Polar BEAR satellites from four ground stations: Bellevue, Washington; Tromso, Norway; Ft. Churchill, Canada; and Sondre Stromfjord, Greenland. Table 8 lists information about each of these five data sets. The column labeled IPP in this table is the geomagnetic (apex) latitude at the 350-km ionospheric penetration point, and is the average for each data set.

3.1 Model Plan. There will be six main stages to the high-latitude upgrade effort:

1. Establish the software and procedures for calculating estimates of $C_k L$ from the various scintillation observations. This has been completed at all stations, but we are concerned about the potential effects of small errors in the satellite locations in the HiLat and Polar BEAR modeling databases on the calculated $C_k L$. These errors are due to the use of outdated ephemeris sets at field sites at times when updated ephemerides were not available. This is discussed further in Section 3.2.
2. Update the geophysical variations, i.e., the variation of $C_k L$ with SSN and K_p .

Ground Station	Satellite	IPP	Dates	Points
Bellevue	HiLat/PB	54.1°	1984-1987	86,240
Poker Flat	WIDEBAND	65.9°	1976-1979	61,340
Tromso	HiLat/PB	67.1°	1984-1987	512,490
Ft. Churchill	HiLat/PB	69.7°	1984-1988	317,090
Sondre Stromfjord	HiLat/PB	74.0°	1984-1988	696,020

Data types —

S_4 : Intensity scintillation index (RMS)
 σ_ϕ : Phase scintillation index (RMS)
 T : Phase PDS spectral strength (1Hz)
 p : Phase PDS spectral slope

Table 8: Data available for use in the high-latitude model upgrade.

3. Update the diurnal variation.
4. Update the seasonal/longitudinal variation. The present WBMOD does not include a seasonal or longitudinal variation as none was found in the WIDEBAND Poker Flat data set. There is evidence of a definite seasonal variation at other longitude sectors, a variation which has been tied to the offset between the geographic and geomagnetic poles. We plan to use the longitude diversity in our data set to address this issue.
5. Implement all changes to the high-latitude model into the research version of WBMOD. This version will be denoted Version 13.00.

3.2 C_kL Calculation. Calculating C_kL from the scintillation observations in the high-latitude database is done using the algorithms developed for the Air Weather Service (AWS) GBCKL program [Secan *et al.*, 1990]. These are essentially the algorithms used in WBMOD to calculate scintillation indices from C_kL run backwards. These algorithms require specification of:

1. Details of the ray path (*i.e.*, the satellite-to-ground geometry). This is calculated using straightforward spherical trigonometry algorithms.
2. Details of the orientation and shape of the plasma-density irregularities which cause the scintillation. This information is not available from observations, so it is calculated

from the models in the current WBMOD for the axial ratios a and b and for the orientation angle δ .

3. The velocity of the line-of-sight with respect to the plasma-density irregularities. There are two components to this: velocity due to motion of either end of the ray path (satellite motion, for example), and the *in-situ* drift velocity of the irregularities. The component due to the satellite motion is calculated using further spherical trigonometry, and the *in-situ* drift is modeled using the drift-velocity model in the current WBMOD.

Estimates of $C_k L$ can be calculated from either S_4 and p , σ_ϕ and p , or T and p . For the modeling effort, we will calculate $C_k L$ from σ_ϕ and S_4 with p from the WIDEBAND data set and from T with p from the HiLat and Polar BEAR data sets.

As stated earlier, there may be a problem in the $C_k L$ values due to errors in the satellite locations stored in the modeling database files. This can cause severe problems when the line-of-sight is passing very nearly parallel to geomagnetic field lines or nearly tangent to L-shells. Scintillation tends to be enhanced at these points, and small errors in calculating the angle between the line-of-sight and the direction of the geomagnetic field can result in non-trivial errors in the calculated $C_k L$. We will be looking into this over the next period by recalculating all satellite locations (HiLat and Polar BEAR) using a large database of ephemerides for these two satellites provided by Dr. Kelso at the US Air Force Institute of Technology.

3.3 Preliminary Results.

3.3.1 Scintillation Boundary. The initial plan for modeling the transition boundary from the mid-latitude to auroral regions was to derive the location and behavior of this boundary directly from the scintillation observations. This has been found to be impossible to do using the large binned data sets we routinely use in the modeling work. The boundary becomes smeared in both latitude and time when many passes are averaged together. There are obvious changes in the average patterns (plots of average $\log(C_k L)$ as a function of latitude and local time) with K_p , but they are very small and difficult to model. The alternatives to extracting the boundary behavior from the aggregate database are (1) to manually inspect a large number of individual passes to determine where the boundary is located in each pass, and (2) to design and test an automated "boundary finder" which will read the passes in the aggregate database and determine boundary locations for each pass. Neither of these tasks is within the scope of the present work.

As a workable alternative, we are going to follow the path used in developing the original WBMOD high-latitude model and use a boundary derived from another data source as the basis for the model of the scintillation boundary. The boundary of choice is that specified by the DMSP SSJ/4 electron-precipitation data, and a model based on those data. As a first look, we looked at the behavior of $\log(C_k L)$ as a function of the location of a precipitation boundary derived from a model. This was promising, so the full SSJ/4 boundary database

was obtained from Dr. Fred Rich (PL/GPSG) to include in our modeling database.

Our choice of the SSJ precipitation boundary was based on several factors. First, there is a large database available of this boundary location covering most of our scintillation database. Second, there is a model available for use in WBMOD which will provide this boundary location as a function of K_p . Finally, this is a parameter which is routinely available at the AFSFC.

The SSJ model used is based on offset circles in geomagnetic latitude and local time fitted to the model of the boundary movement as a function of K_p presented in *Gussenhoven et al. [1983]*. In that paper, they presented different linear functions of the boundary latitude with K_p for each local geomagnetic time. The present model defines the boundary location with the radius and center (latitude and local time) as functions of K_p . These three models are as follows:

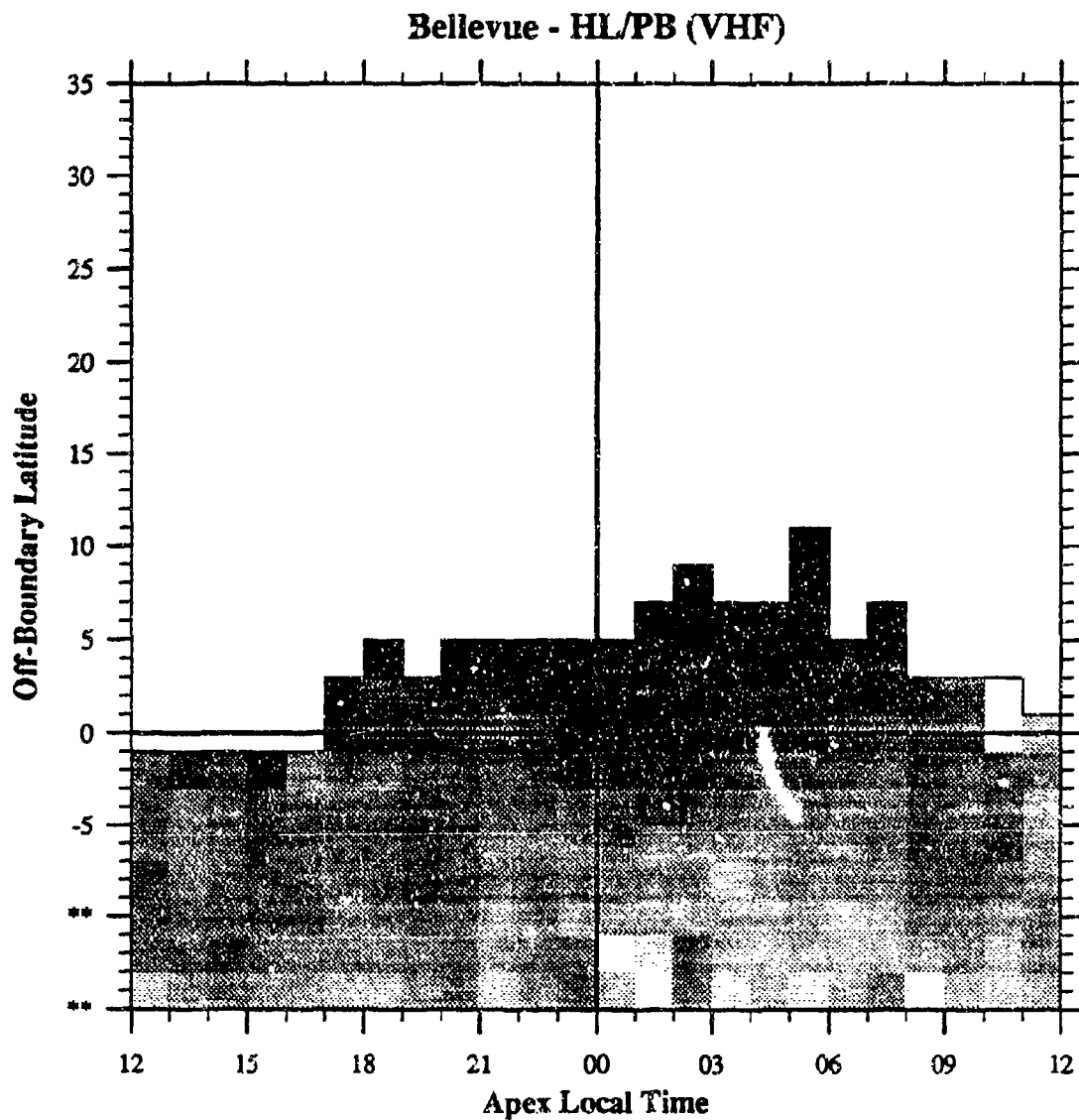
$$\begin{aligned} R &= 20.97 + 1.658K_p \quad \text{degrees} \\ L &= 2.466 + 0.3651K_p \quad \text{degrees} \\ \Phi &= 2.862 - 0.09638K_p + 0.004893K_p^2 \quad \text{hours} \end{aligned} \tag{17}$$

This model has been used in the WBMOD high-latitude drift velocity model since Version 10H1 to specify the behavior of the drift velocity equatorward of the reversal boundary.

The SSJ/4 boundary database provided by Dr. Rich is the boundary location interpolated from the local time of observation to local geomagnetic midnight. This database covers the years 1983 through 1991 (all of the HiLat and Polar BEAR data sets, but none of the WIDEBAND data set), and contains over 122,000 data points.

To determine the behavior of the scintillation boundary, we will study the variation of $C_k L$ with respect to the location of the precipitation boundary. This should remove, at least to first order, K_p -dependent effects in the scintillation due to motion of the boundary. [Note: Recall that WBMOD is a climatological model, and not a phenomenological one. While this last statement is workable for a climatological model, it is not necessarily true for individual cases. The scintillation boundary is most likely less dynamic than the precipitation boundary.]

We have just begun to work on this study, but the preliminary results are very promising. Figures 7 through 11 show the variation $\log(C_k L)$ (averaged in one-degree by 1-hour bins) as a function of distance from the precipitation boundary (in geomagnetic latitude) and apex (geomagnetic) local time. The boundary locations for all of the HiLat and Polar BEAR data were derived from the boundary database. Only boundaries observed within



X-axis bin size: 1.00

Z parameter: $\log(C_k L)$ [from S4]

Y-axis bin size: 2.00

Z min: 30.5 Z max: 32.5

Number of data points: 32518

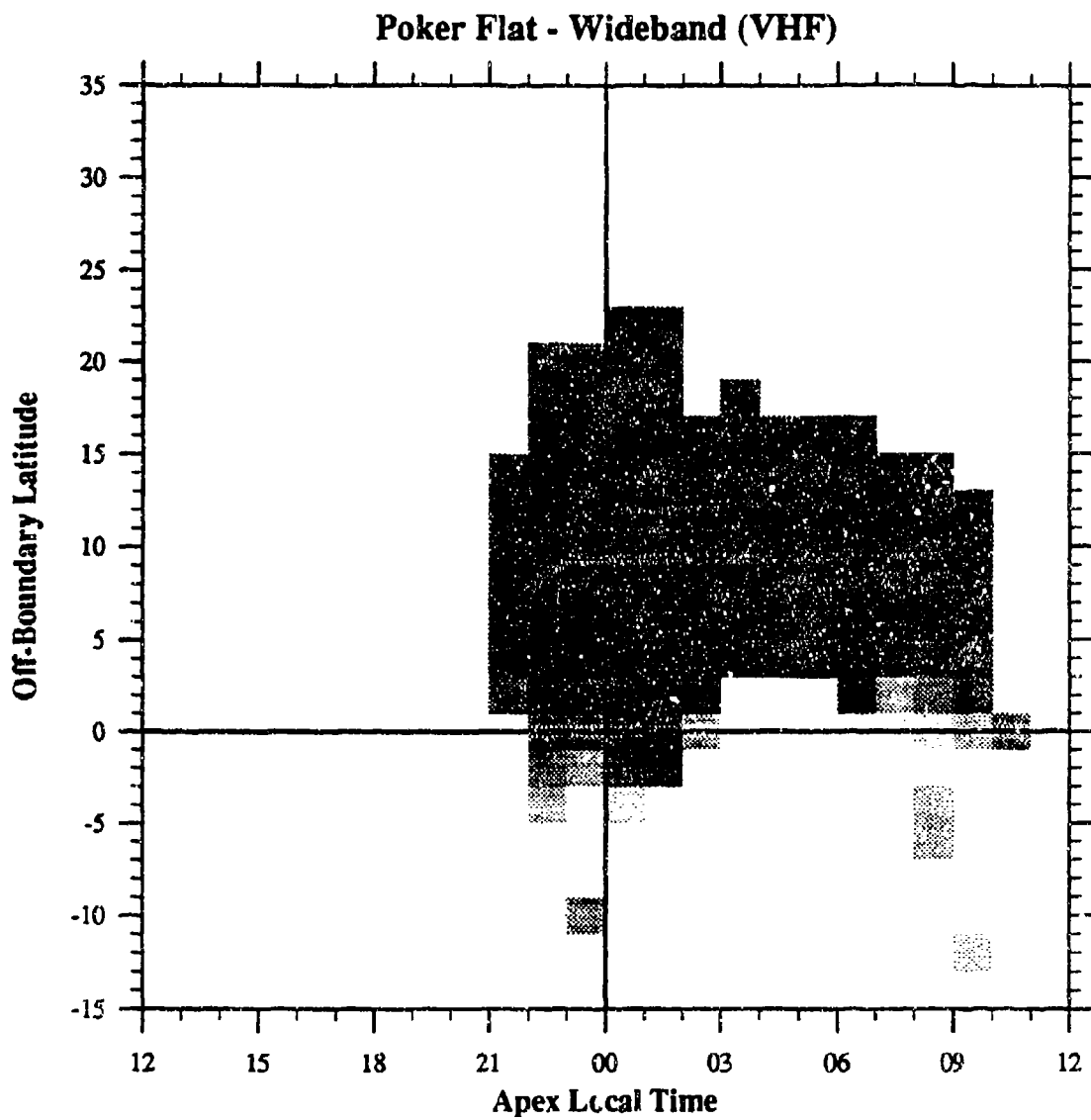
White: 30.5 Black: 32.5

Data limited to $1.5 < p < 4.5$

Data limited to $\Theta > 65^\circ$

VDRIFT from WBMOD model

Figure 7: Bin-averaged behavior of $\log(C_k L)$ at Bellevue as a function of the distance in geomagnetic latitude from the high-latitude precipitation boundary and geomagnetic local time. The boundary location was derived from the DMSP SSJ boundary database.



X-axis bin size: 1.00

Y-axis bin size: 2.00

Number of data points: 21876

Z parameter: $\log(C_k L)$ [from S4]

Z min: 29.8 Z max: 32.7

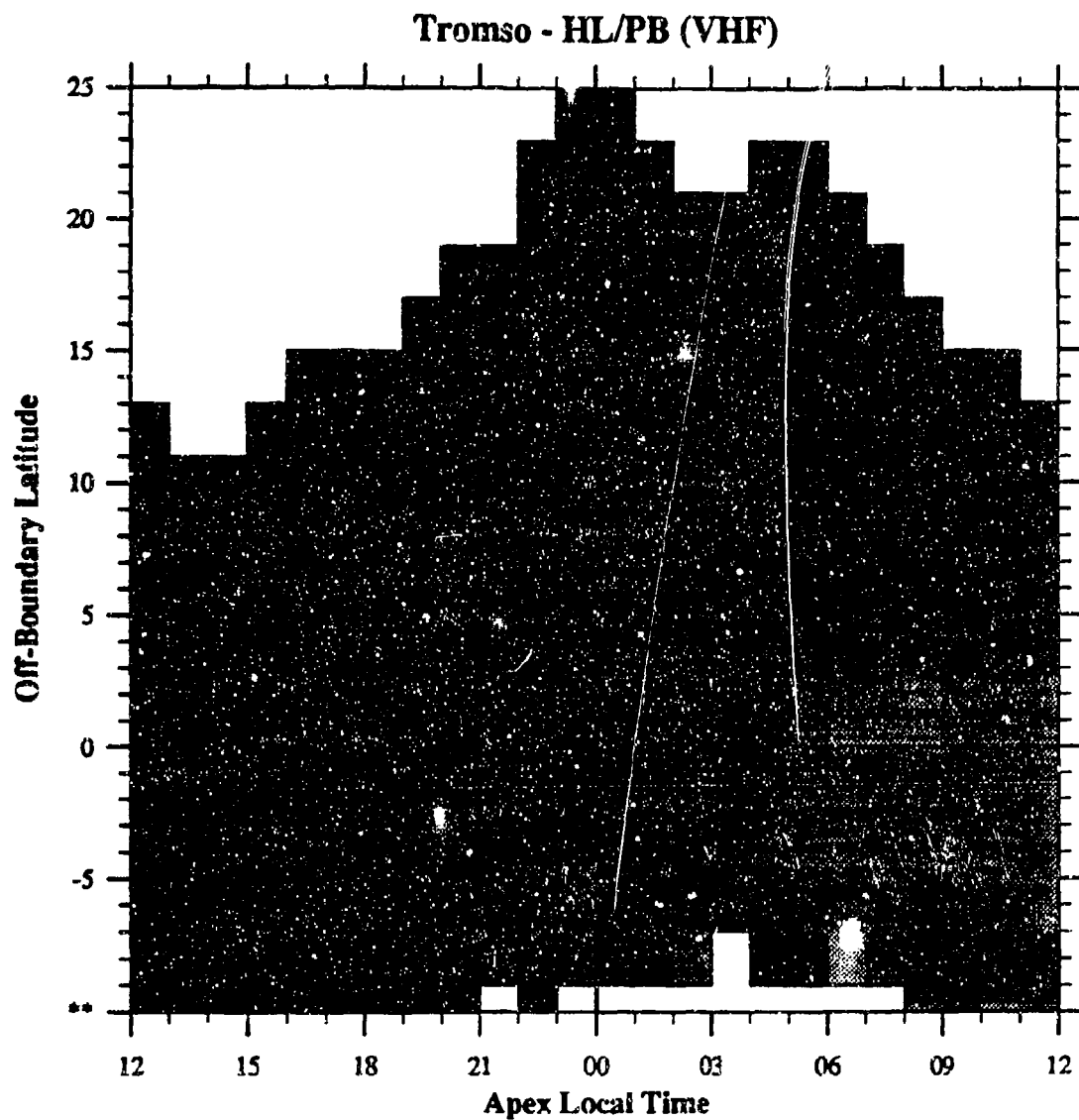
White: 30.5 Black: 32.5

Data limited to $1.5 < p < 4.5$

Data limited to $\Theta > 65\text{deg}$

VDRIFT from WBMOD model

Figure 8: Bin-averaged behavior of $\log(C_k L)$ at Poker Flat as a function of the distance in geomagnetic latitude from the high-latitude precipitation boundary and geomagnetic local time. The boundary location was derived from the K_p -dependent model described in the text.



X-axis bin size: 1.00

Y-axis bin size: 2.00

Number of data points: 181227

Z parameter: $\log(C_k L)$ [from S4]

Z min: 30.8 Z max: 32.8

White: 30.5 Black: 32.5

Data limited to $1.5 < p < 4.5$

Data limited to $\Theta > 65\text{deg}$

VDRIFT from WBMOD model

Figure 9: Bin-averaged behavior of $\log(C_k L)$ at Tromso as a function of the distance in geomagnetic latitude from the high-latitude precipitation boundary and geomagnetic local time. The boundary location was derived from the DMSP SSJ boundary database.

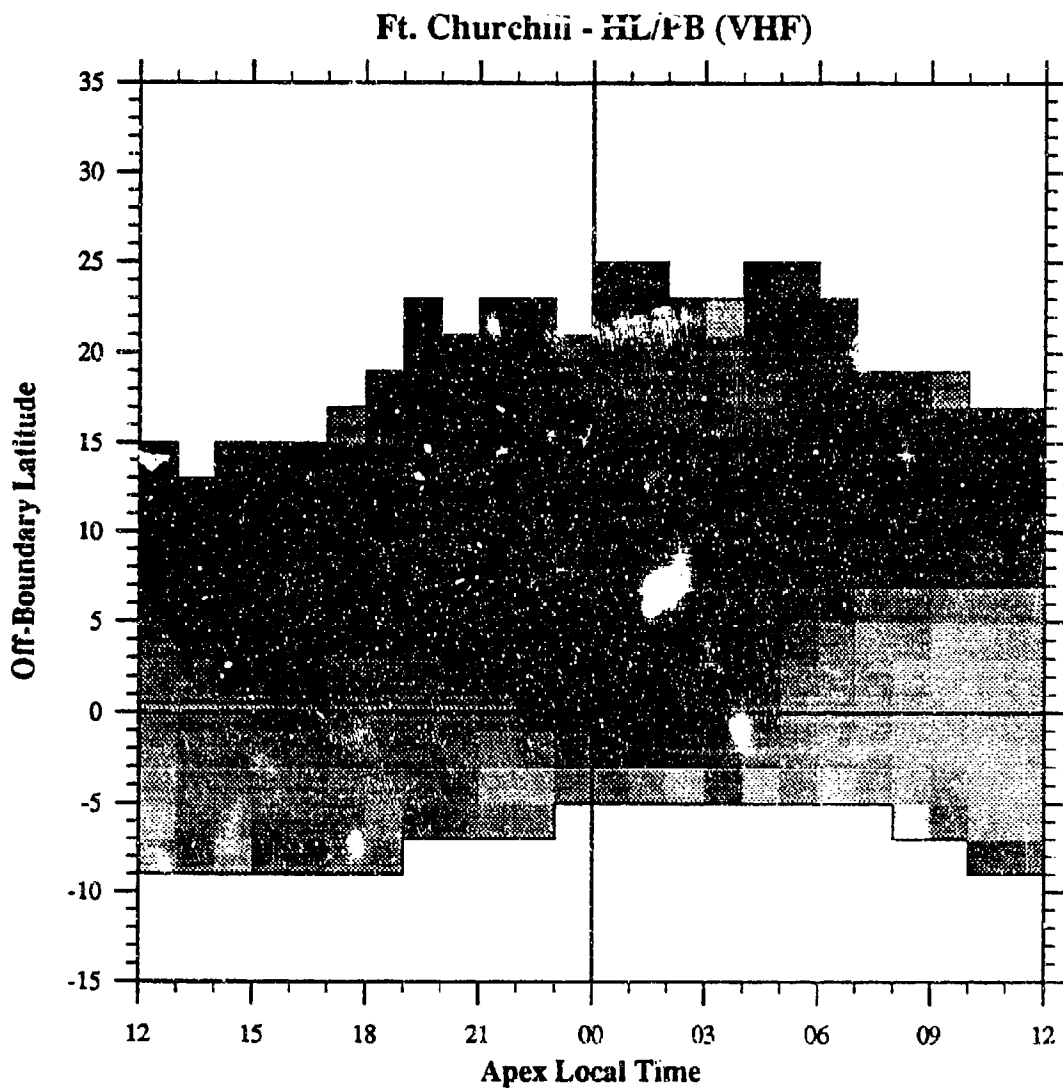
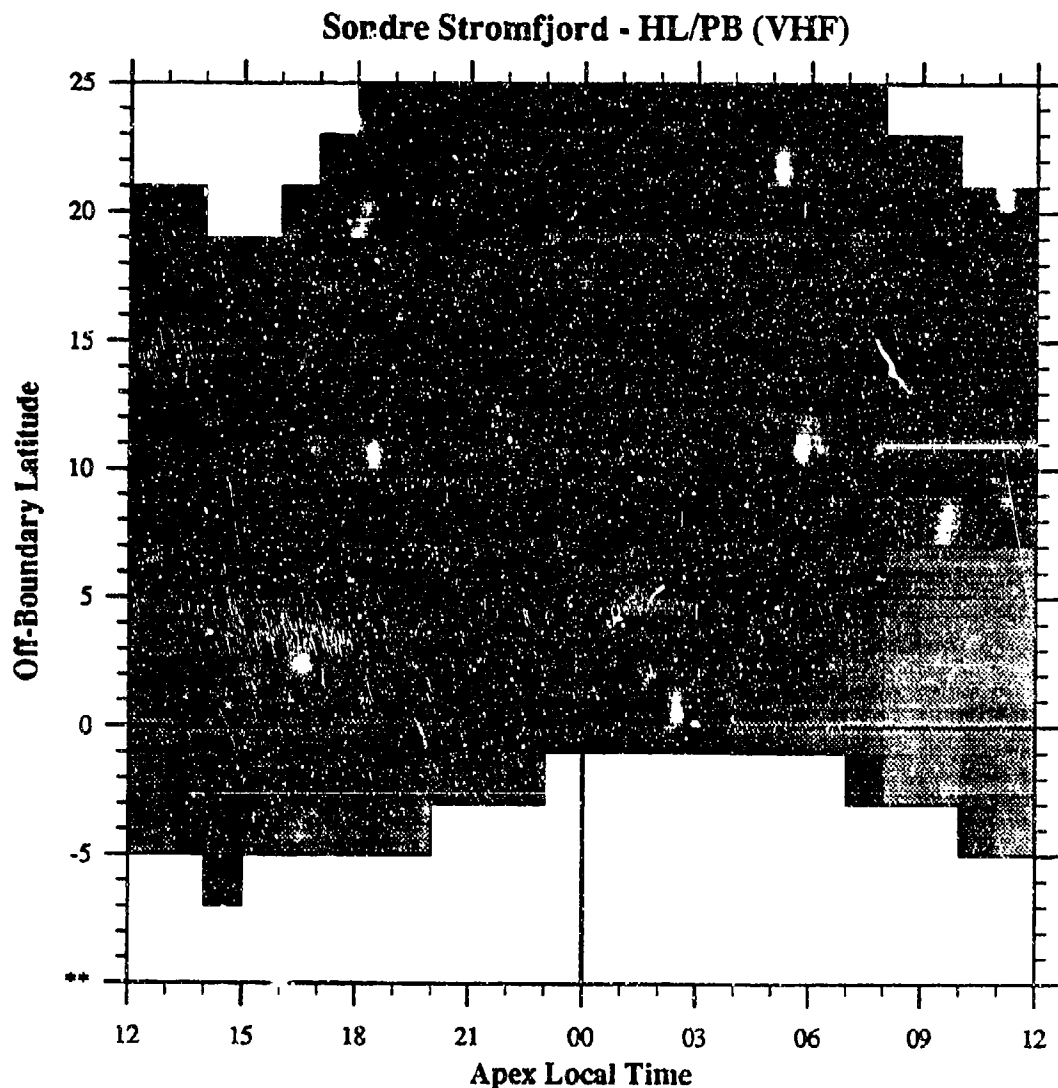


Figure 10: Bin-averaged behavior of $\log(C_k L)$ at Ft. Churchill as a function of the distance in geomagnetic latitude from the high-latitude precipitation boundary and geomagnetic local time. The boundary location was derived from the DMSP SSJ boundary database.



X-axis bin size: 1.00

Y-axis bin size: 2.00

Number of data points: 236213

Z parameter: $\log(C_{kL})$ [from S4]

Z min: 30.8 Z max: 32.4

White: 30.5 Black: 32.5

Data limited to $1.5 < p < 4.5$

Data limited to $\Theta > 65\text{deg}$

VDRIFT from WBMOD model

Figure 11: Bin-averaged behavior of $\log(C_{kL})$ at Sondre Stromfjord as a function of the distance in geomagnetic latitude from the high-latitude precipitation boundary and geomagnetic local time. The boundary location was derived from the DMSP SSJ boundary database.

30 minutes of the scintillation observation were used. The boundary location for the Poker Flat (WIDEBAND) data set was calculated using K_p and the SSJ boundary model. All of these plots show systematic behavior with respect to the precipitation boundary, which shows promise for the modeling effort.

3.3.2 K_p Variations. The current high-latitude $C_k L$ model moves the location (latitudinal extent) and transition-width ("steepness" of the transition) of the scintillation boundary as a function of K_p . This boundary moves equatorward with K_p and the width increases accordingly. The $C_k L$ value at a fixed station increases with increasing K_p solely due to the motion of the boundary. The level of $C_k L$ within the high-latitude region does not change as a function of K_p .

Our preliminary study shows that this is in rough agreement with the present data set, although we do see some increase in $C_k L$ with increasing K_p for locations which are well within the boundary location. We will be looking closely at this to determine if this is a real effect, or a residual effect of errors in locating the boundary.

3.3.3 SSN Variations. All of the data sets show a general increase in scintillation levels with increasing SSN. This is not surprising since the overall ionospheric density is known to increase with increasing SSN. Our initial results, however, show that the increase of $C_k L$ with SSN is slower than that in the present WBMOD. The current model shows $\log(C_k L)$ increasing as 0.017 times the SSN, while the initial analysis of the data at hand shows only an increase of 0.005 times the SSN. Re-analysis of the WIDEBAND data from Poker Flat (which was the only data set used in the original modeling) agrees with this new value for the variation with SSN. We are, at this time, at a loss to explain this discrepancy. We have seen evidence for a slightly different variation with SSN in different latitude and local-time regimes. We will investigate this further.

4. Conclusion

The upgrade to the equatorial region of the WBMOD $C_k L$ model has been completed, and the upgrade has been implemented in the research version of WBMOD (Version 12). A User's Guide has been written which provides a brief description of the model, and describes how the model should be run and the inputs requested by the model as it runs.

Work has begun on the upgrade to the high-latitude $C_k L$ model. This upgrade will use data from the WIDEBAND (Poker Flat), and HiLat/Polar BEAR (Bellevue, Tromso, Ft. Churchill, Sondre Stromfjord) experiments. When the high-latitude model is completed, the new algorithms will be implemented into the research version of WBMOD (Version 13).

REFERENCES.

Aarons, J., Construction of a model of equatorial scintillation intensity, *Radio Sci.*, 20, 397-402, 1985.

Basu, S., S. Basu, and B. K. Kahn, Model of equatorial scintillations from in-situ measurements, *Radio Sci.*, 11, 821-832, 1976.

Fremouw, E. J. and A. Ishimaru, Intensity scintillation index and mean apparent radar cross section on monostatic and bistatic paths, *Radio Sci.*, 27, 539-543, 1992.

Gussenhoven, M. S., D. A. Hardy, and N. Heinemann, Systematics of the equatorward diffuse auroral boundary, *J. Geophys. Res.*, 88, 5692-5708, 1983.

Maruyama, T and N. Matuura, Longitude variability of annual changes in activity of equatorial spread *F* and plasma bubbles, *J. Geophys. Res.*, 89, 10,903-10,912, 1984.

Secan, J. A., Development of Advanced Ionospheric Models in Support of Space-Based Radar Design Studies, Phase II, *NWRA-CR-88-R037*, Northwest Research Associates, Inc., Bellevue, WA, 1989.

Secan, J. A., WBMOD Ionospheric Scintillation Model — An Abbreviated User's Guide, *NWRA-CR-93-R098*, Northwest Research Associated, Inc., Bellevue, WA, 1993.

Secan, J. A., E. J. Fremouw, and R. E. Robins, A review of recent improvements to the WBMOD ionospheric scintillation model, in *The Effect of the Ionosphere on Communications, Navigation, and Surveillance Systems*, Proceedings of the Fifth Ionospheric Effects Symposium, J. Goodman, ed., 607-616, 1987.

Secan, J. A., M. P. Baldwin, L. A. Reinleitner, Real-Time Scintillation Analysis System, Technical Description, *NWRA-CR-89-R049*, Volume 1, Northwest Research Associates, Inc., Bellevue, WA, 1990.

Secan, J. A., R. M. Bussey, E. J. Fremouw, and L. A. Reinleitner, An Investigation of Methods For Improving Models of Ionospheric Plasma-Density Irregularities and Radio-Frequency Scintillation, *PL-TR-93-2050*, ADA264156, Phillips Laboratory, Hanscom AFB, MA, 1993a. **ADA264156**

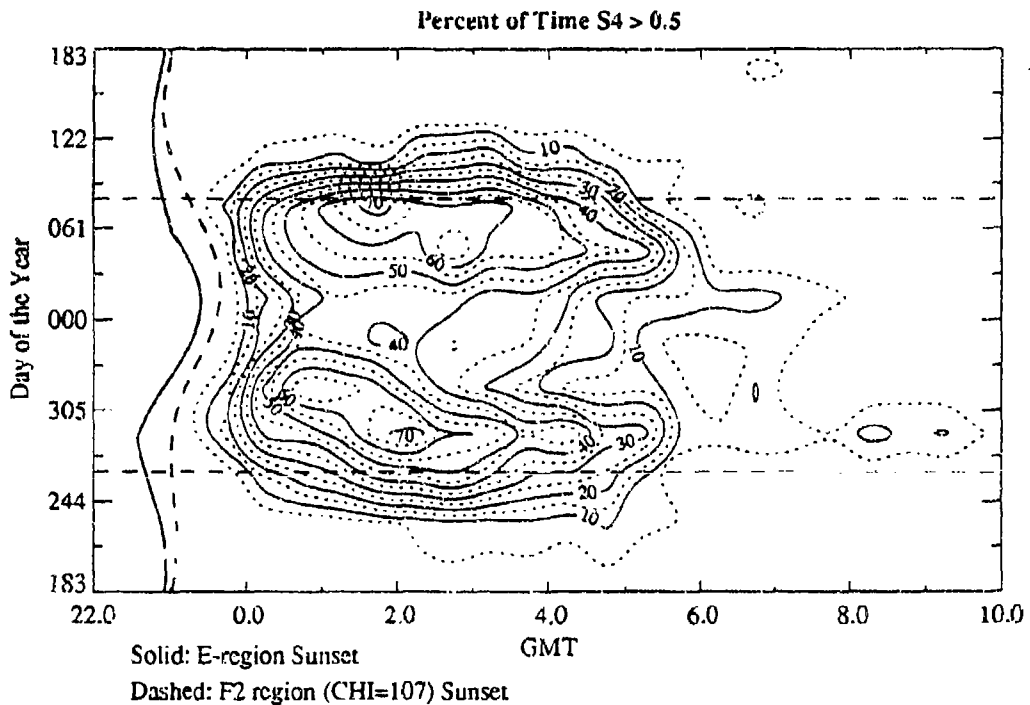
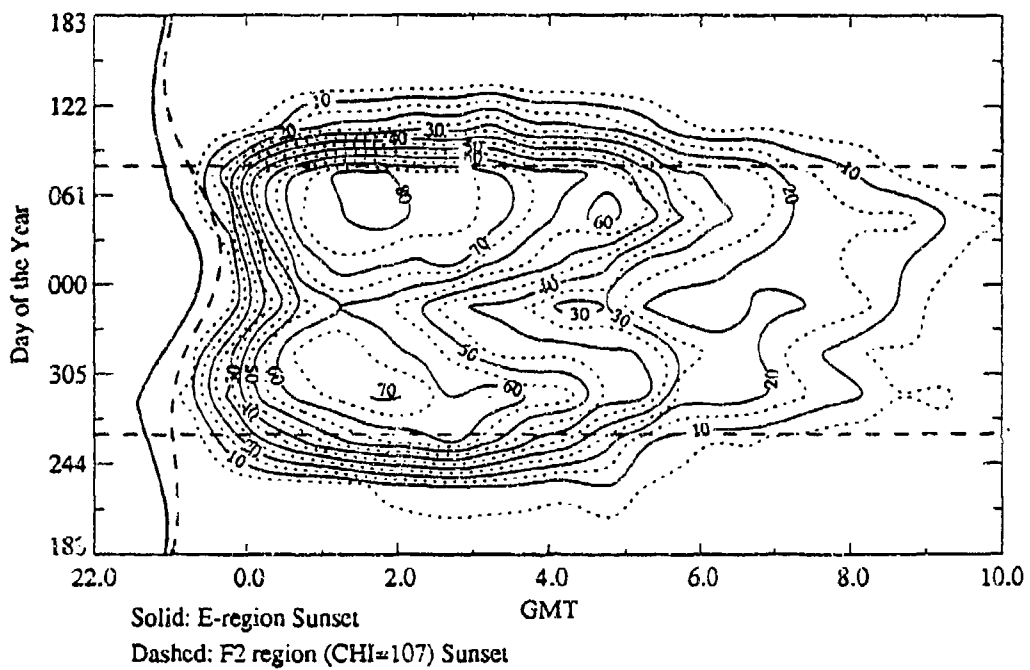
Secan, J. A., R. M. Bussey, E. J. Fremouw, and S. Basu, An improved model of equatorial scintillation, submitted to *Radio Sci.*, 1993b.

Appendix A. Data Plots — Variation with Solar Cycle

The figures in this appendix illustrate how the diurnal/seasonal pattern of occurrence statistics ($S_4 > 0.5$) varies as a function of SSN at Huancayo (VHF), Manila (VHF), and Ascension Island (L-band). There are six plots for each station, one for each of six ranges of SSN : All SSN , $SSN \leq 50$, $50 < SSN \leq 100$, $100 < SSN \leq 150$, $150 < SSN \leq 200$, and $SSN > 200$. In all plots, the data have been limited to those cases for which $KpSS \leq 20$. The bin size in all plots is 30 minutes in GMT by 30.5 days (one month) in day of the year.

The heavy solid line on each plot shows the variation of the time at which both E-region ends of the IPP field line with day of the year, and the heavy dashed line shows the variation of the time at which F2-layer sunset occurs (defined as $\chi = 107^\circ$). The horizontal dashed lines indicate the equinoxes.

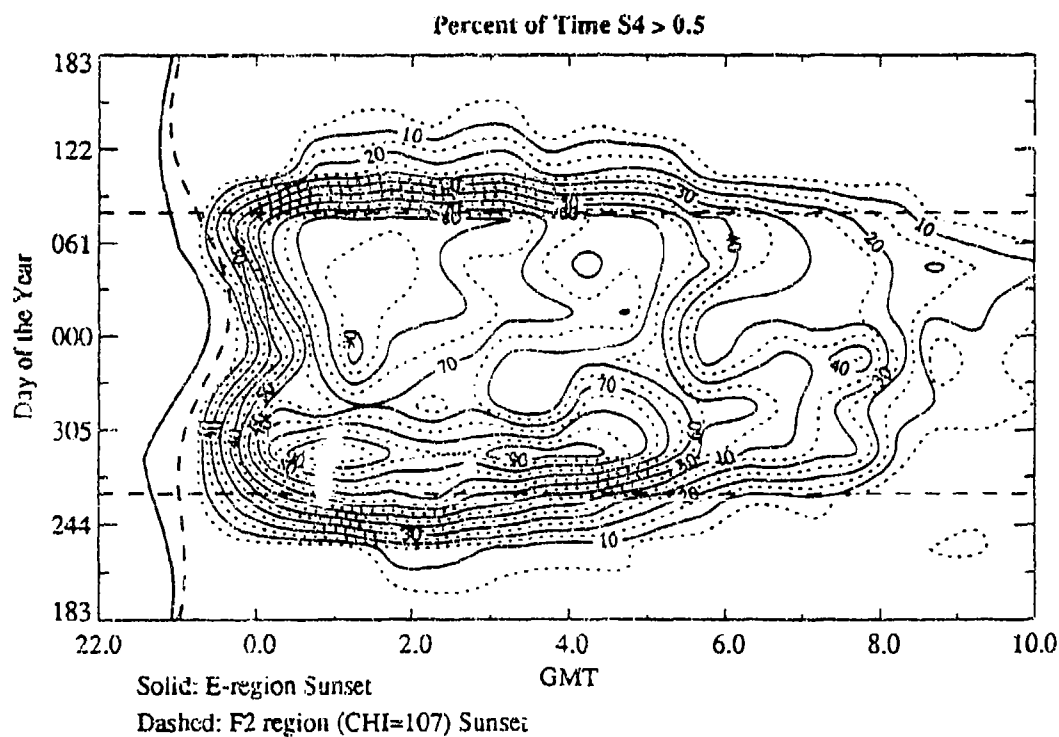
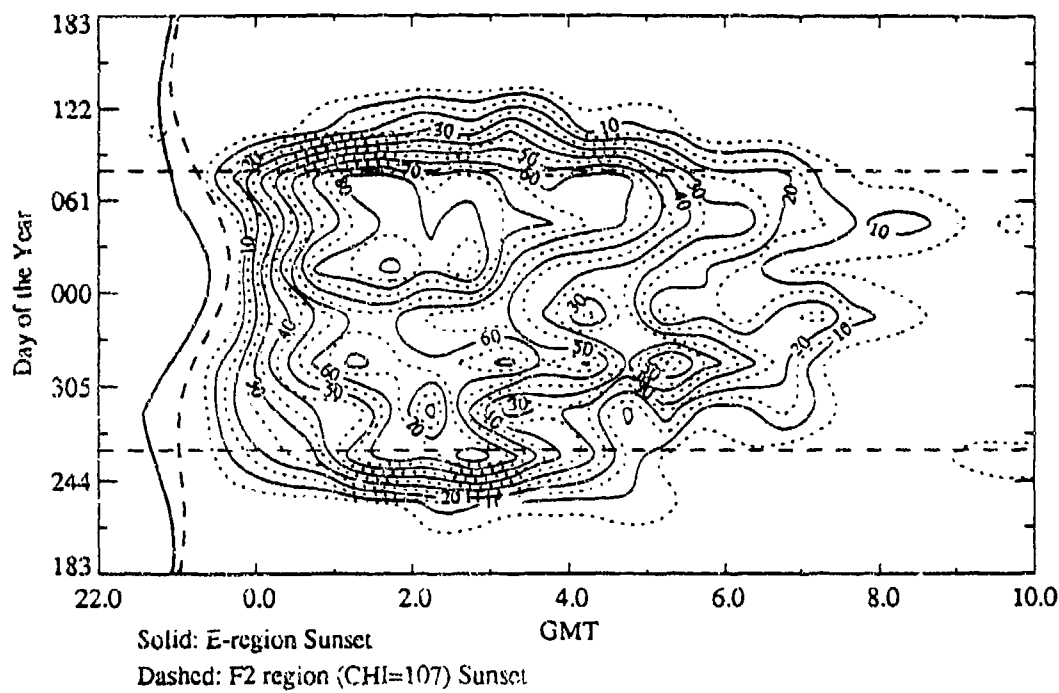
Huancayo-MARISAT (VHF)



All SSN
Kp(SS) <= 20
Total Points: 56,746
Points > 0.5: 9,995

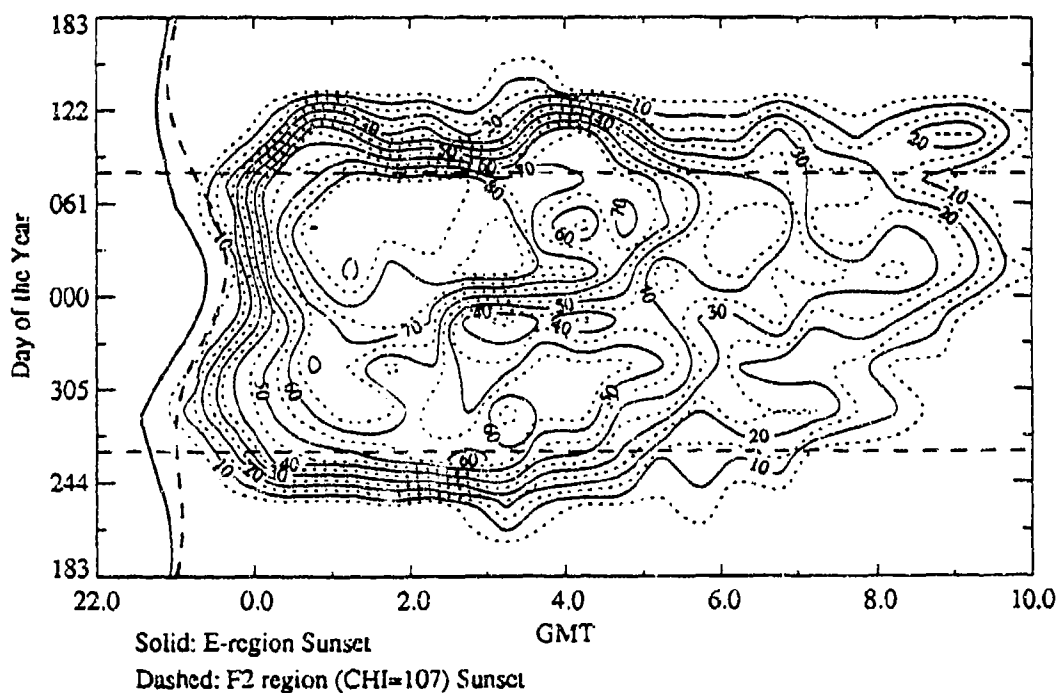
Huancayo-MARISAT (VHF)

Percent of Time $S4 > 0.5$



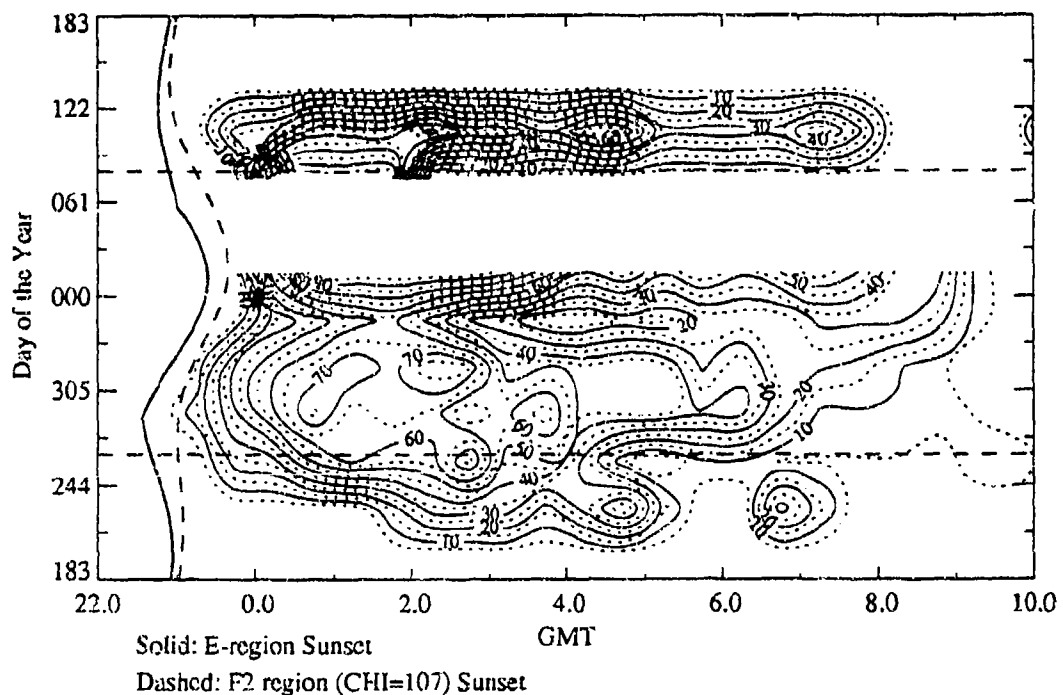
Huancayo-MARISAT (VHF)

Percent of Time $S4 > 0.5$



150 < SSN <= 200
Kp(SS) <= 20
Total Points: 8,01
Points > 0.5: 2,103

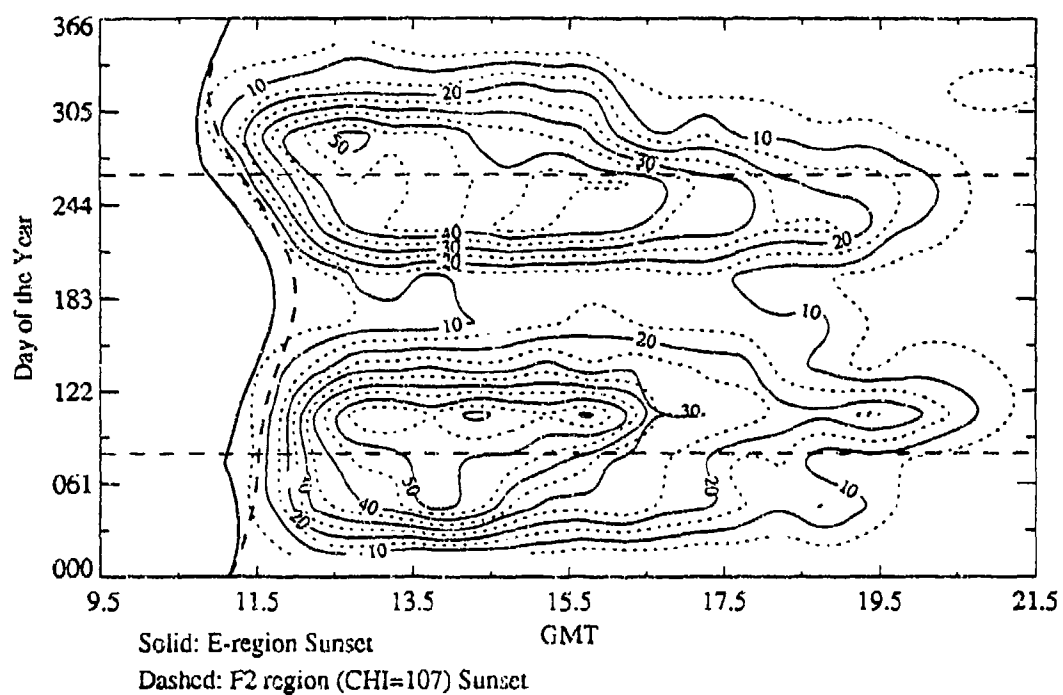
Percent of Time $S4 > 0.5$



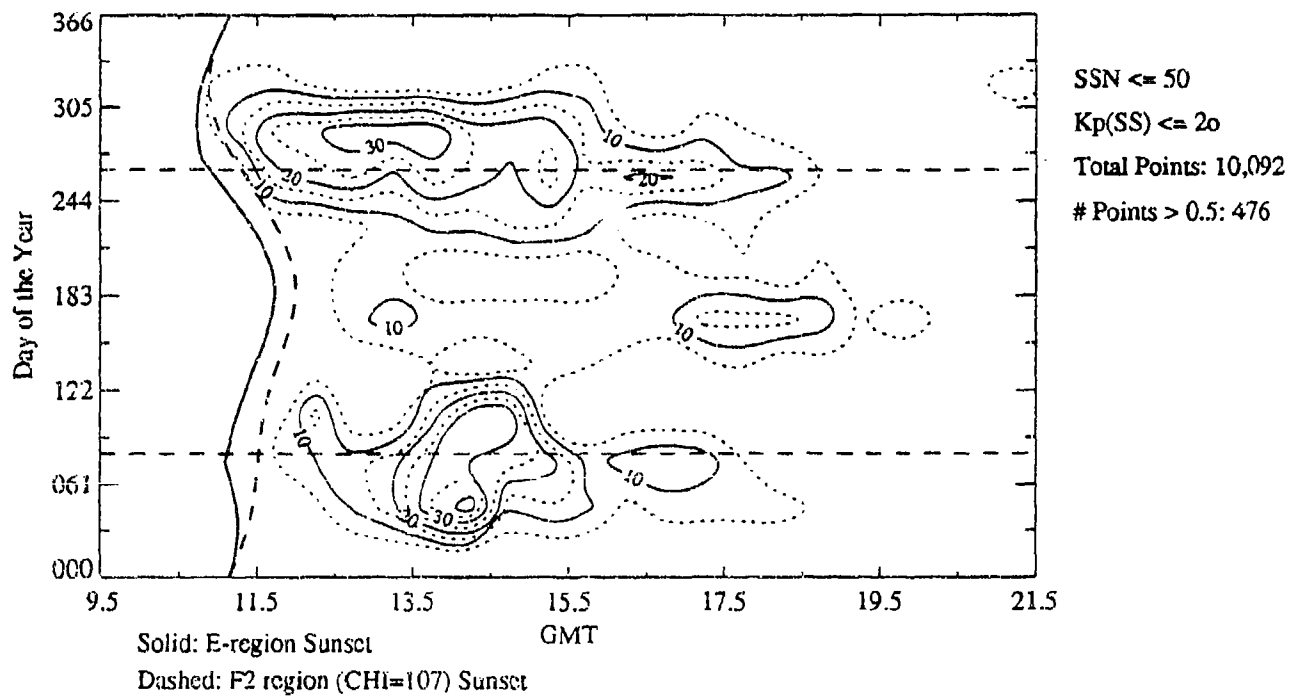
SSN > 200
Kp(SS) <= 20
Total Points: 3,664
Points > 0.5: 947

Manila-FLEETSAT (VHF)

Percent of Time $S4 > 0.5$

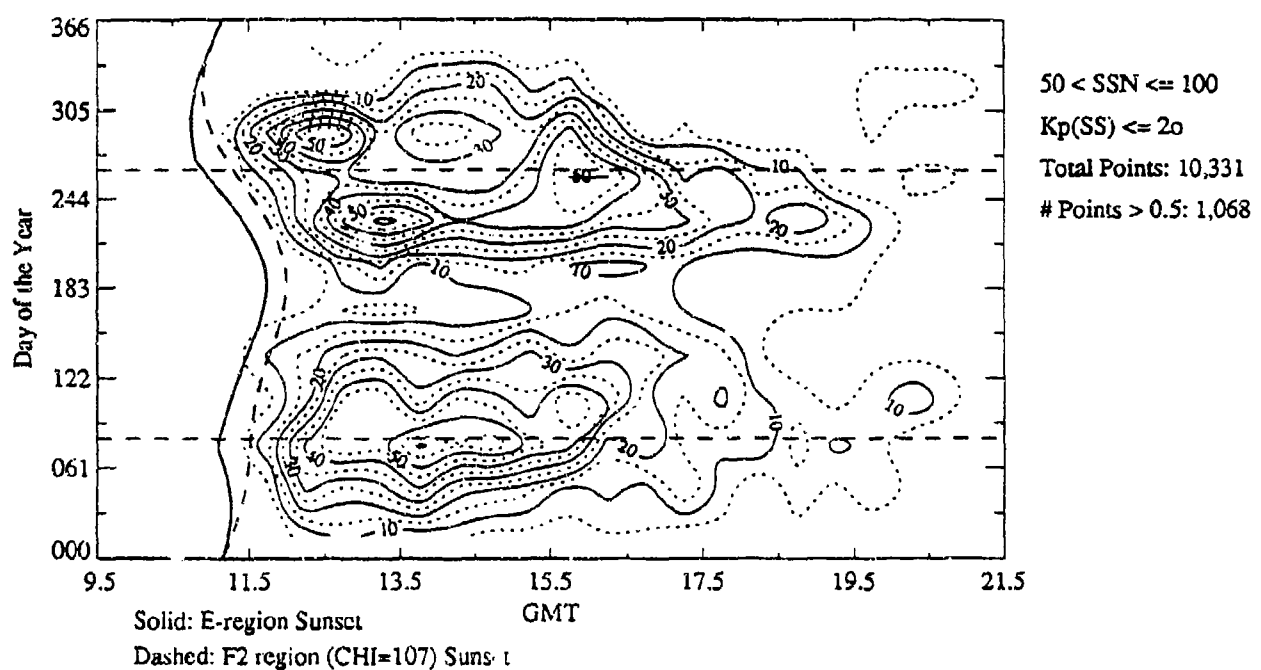


Percent of Time $S4 > 0.5$

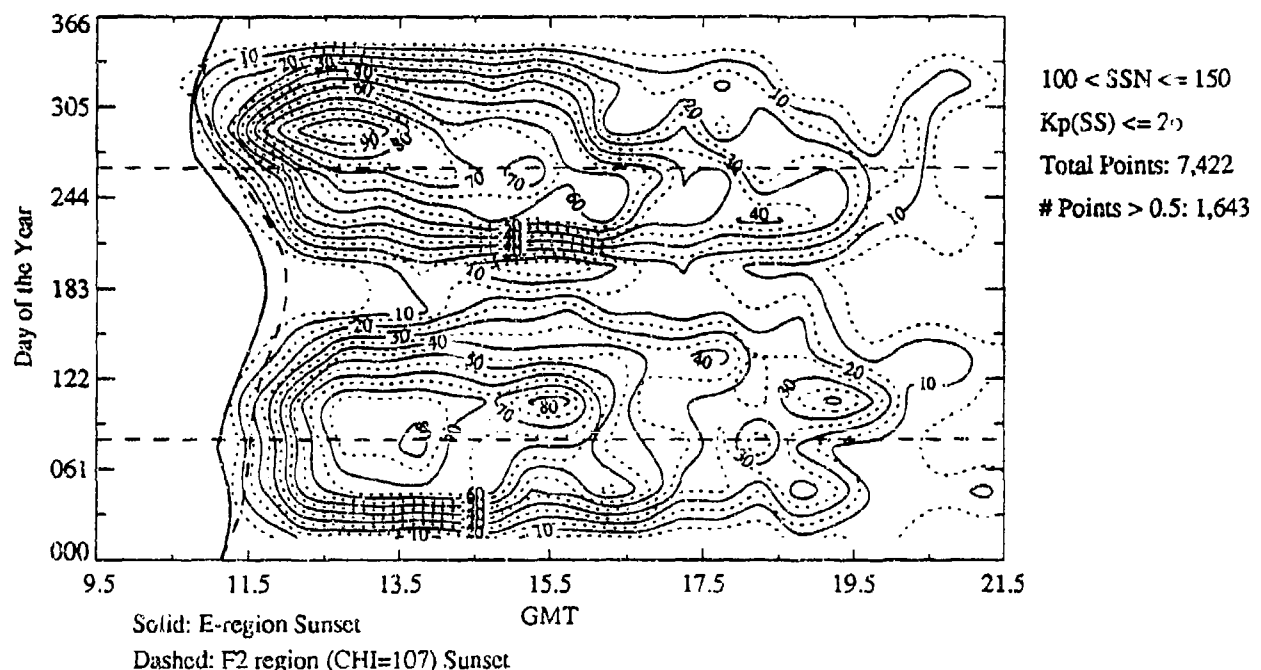


Manila-FLEETSAT (VHF)

Percent of Time $S4 > 0.5$

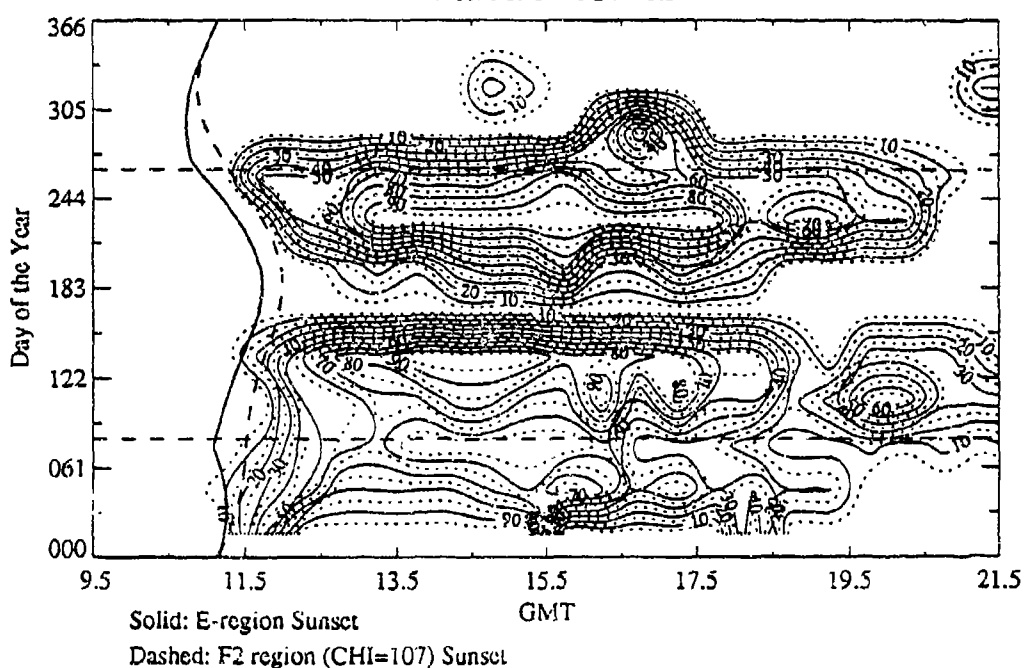


Percent of Time $S4 > 0.5$

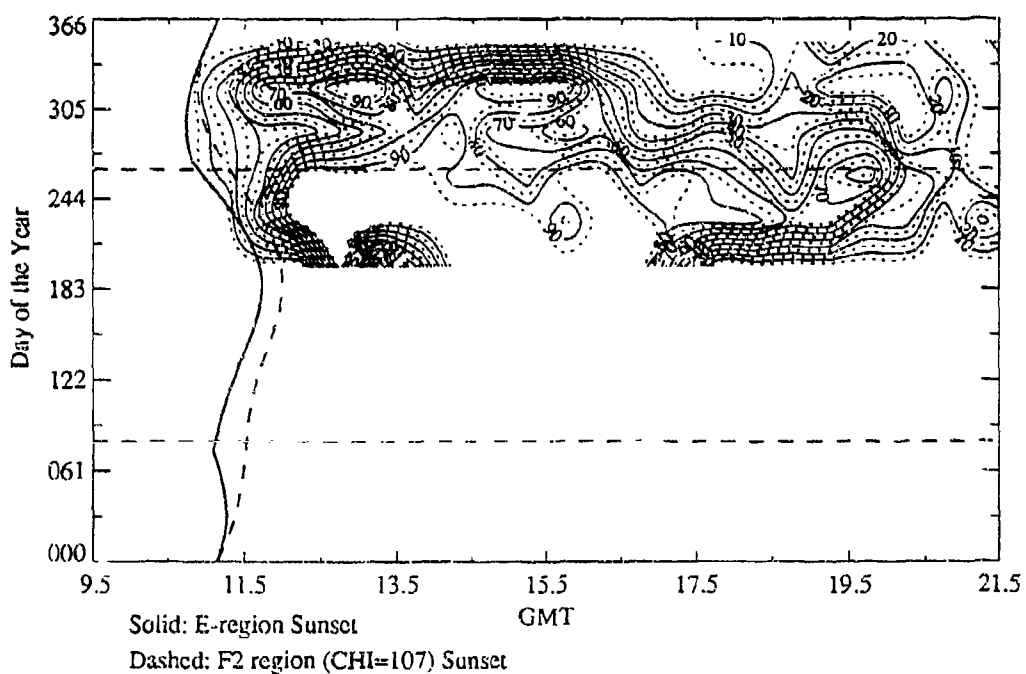


Manila-FLEETSAT (VHF)

Percent of Time $S4 > 0.5$

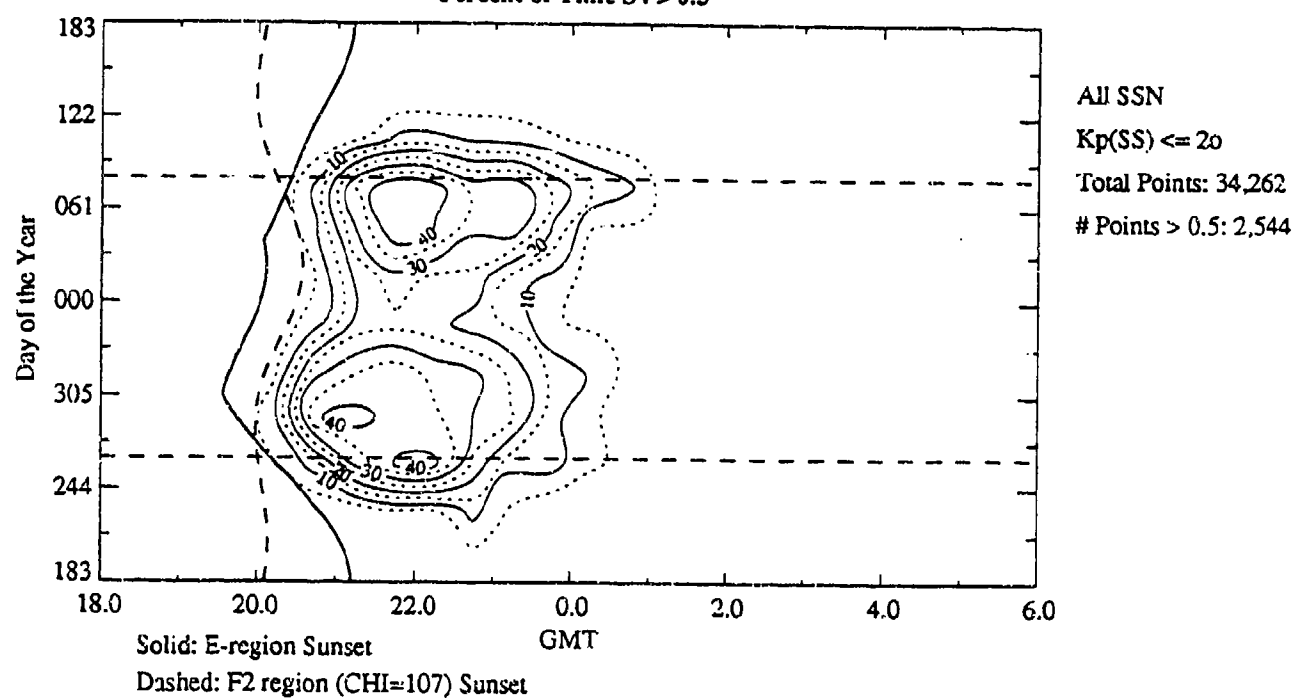


Percent of Time $S4 > 0.5$

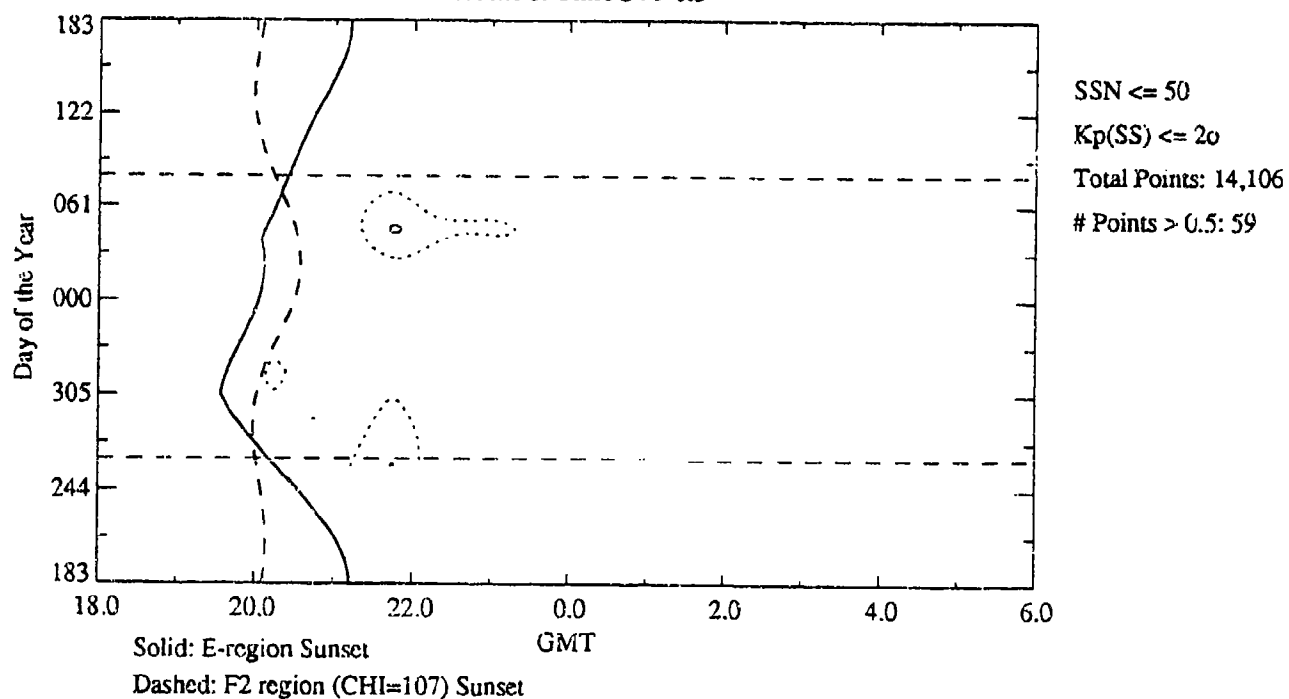


Ascension Is.-MARISAT (L-band)

Percent of Time S4 > 0.5

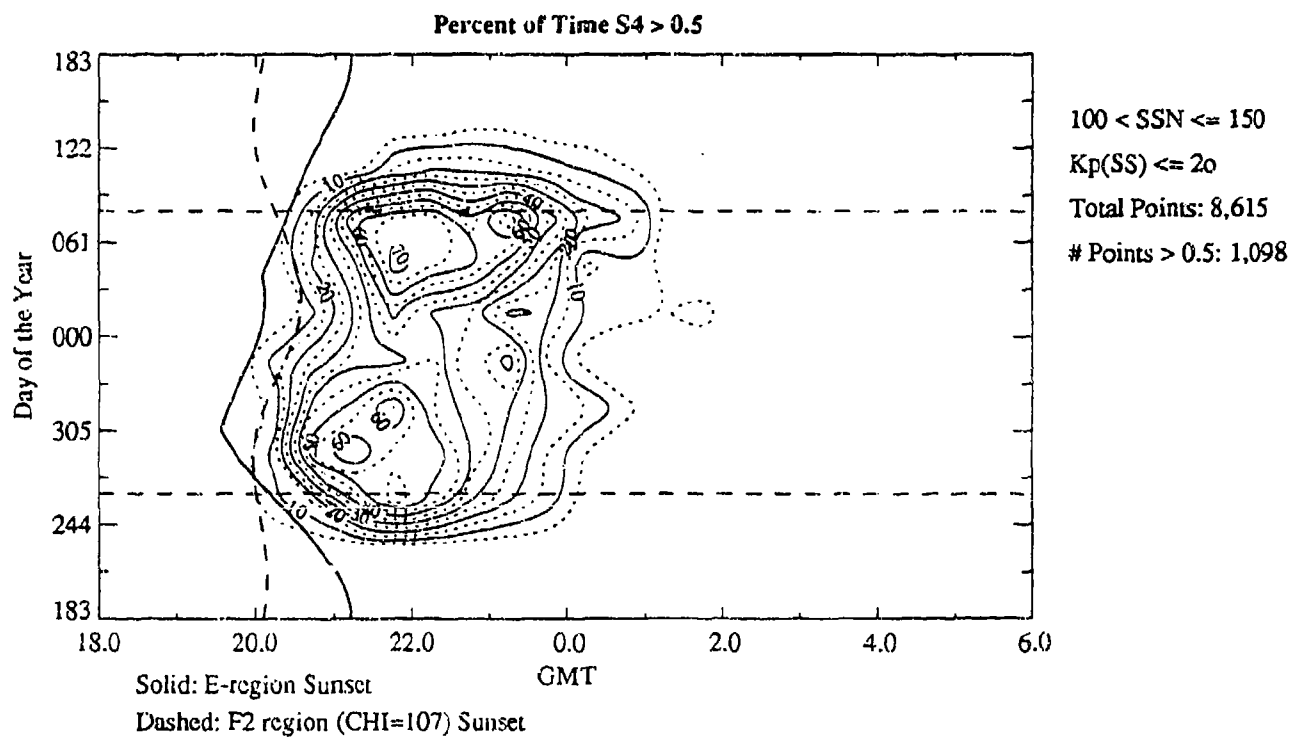
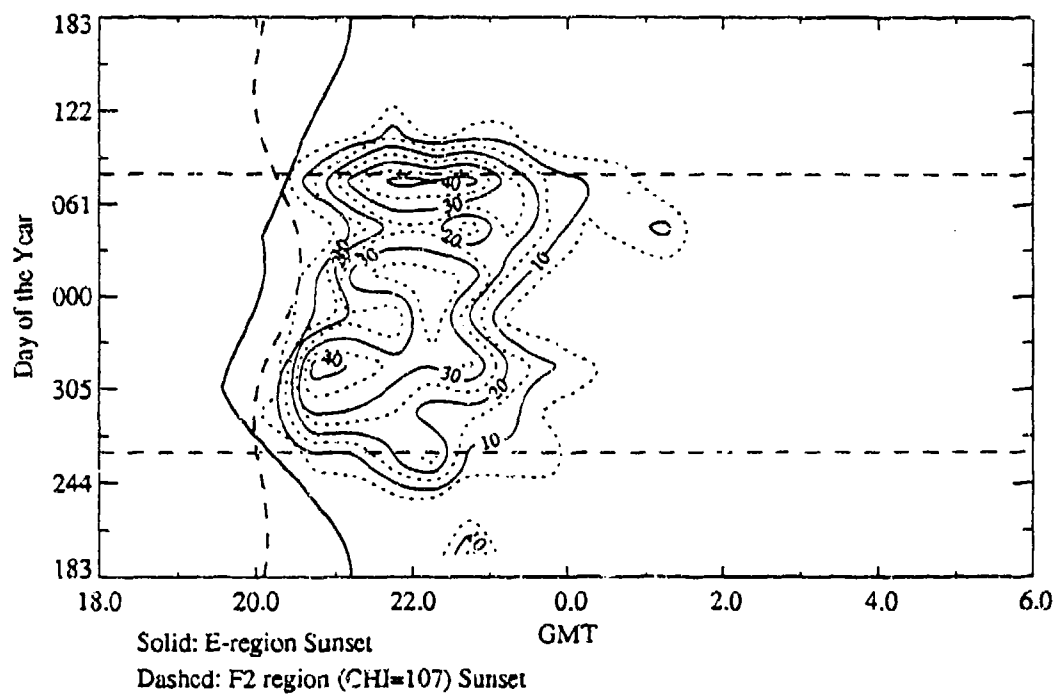


Percent of Time S4 > 0.5



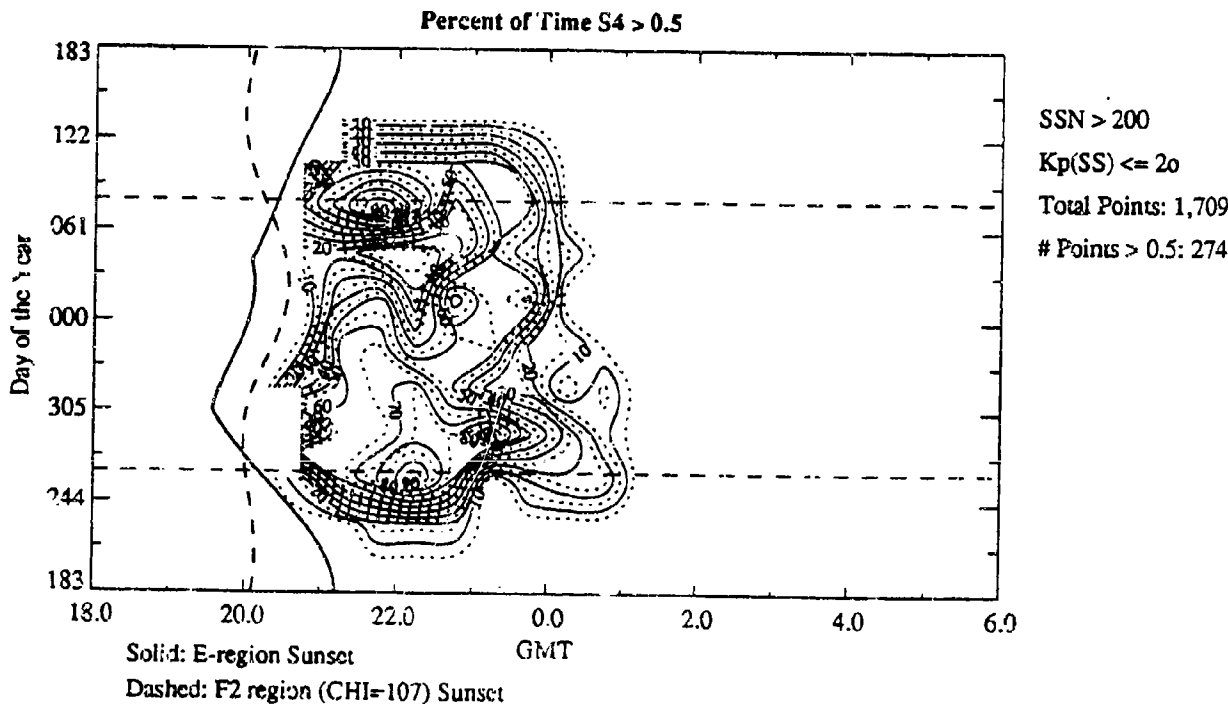
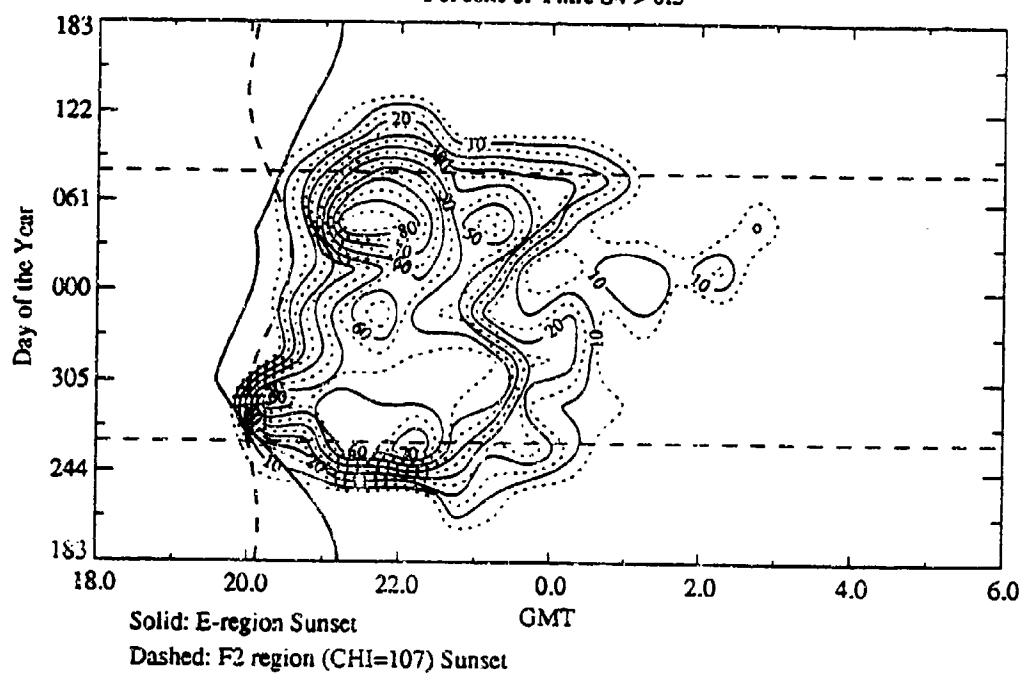
Ascension Is.-MARISAT (L-band)

Percent of Time S4 > 0.5



Ascension Is.-MARISAT (L-band)

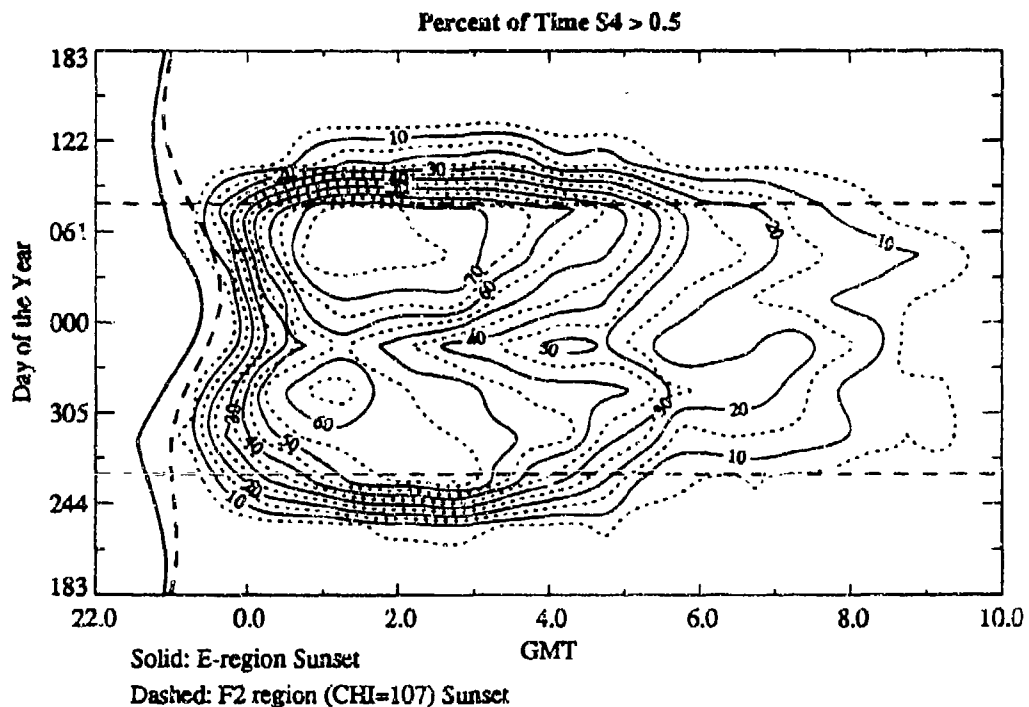
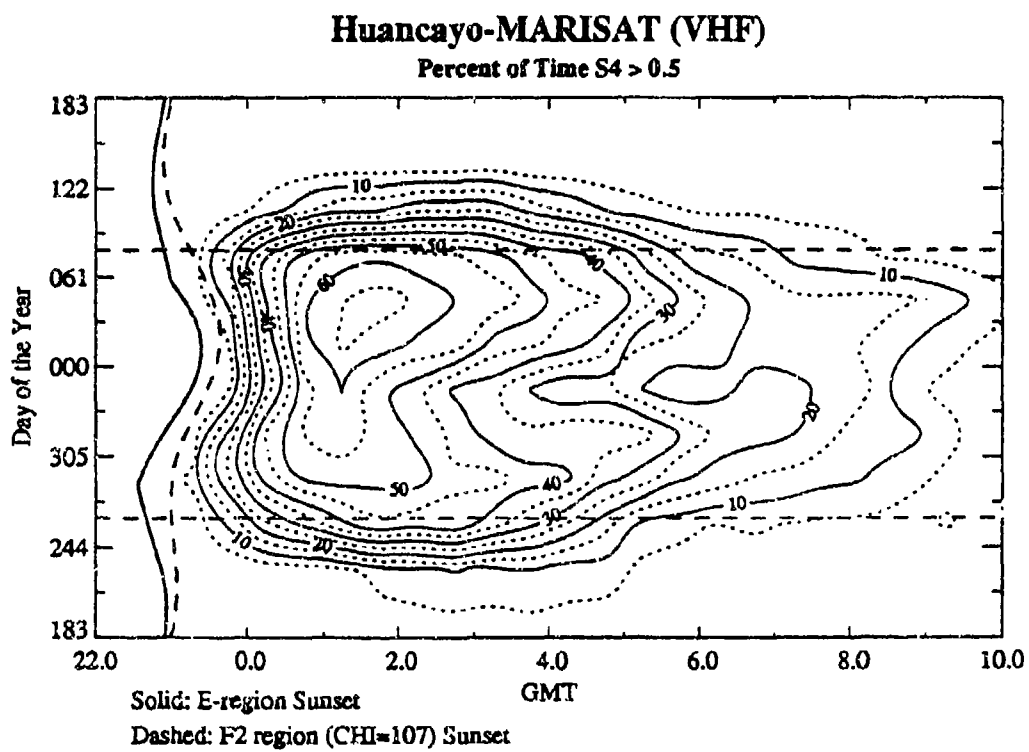
Percent of Time $S4 > 0.5$



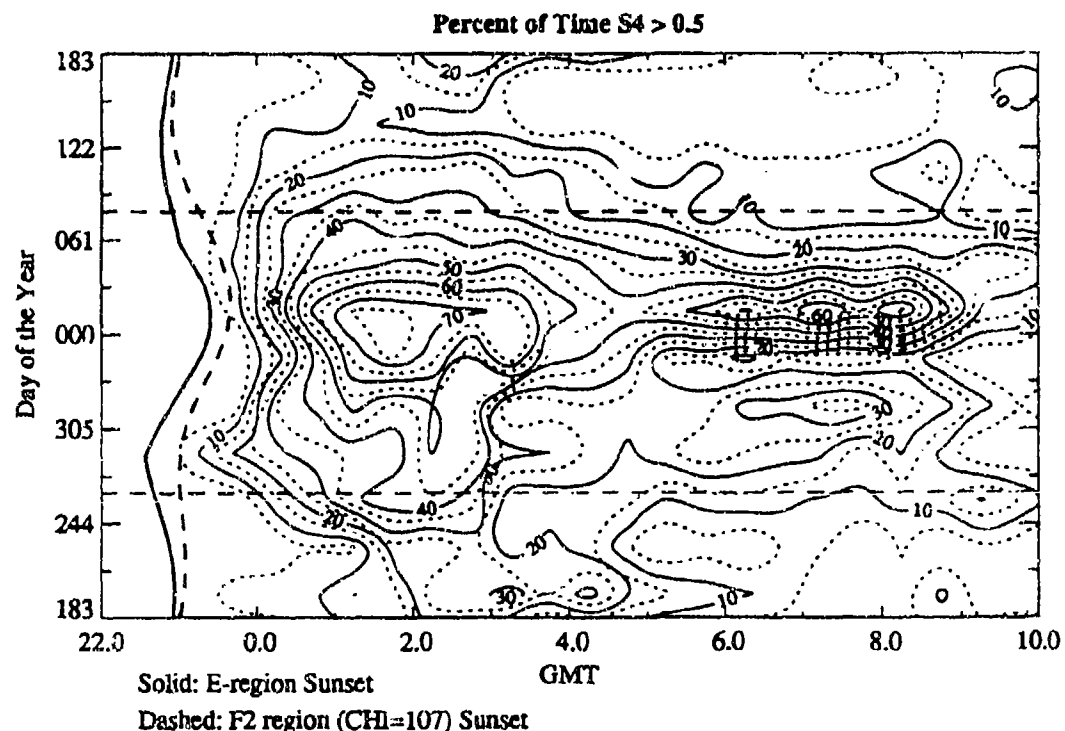
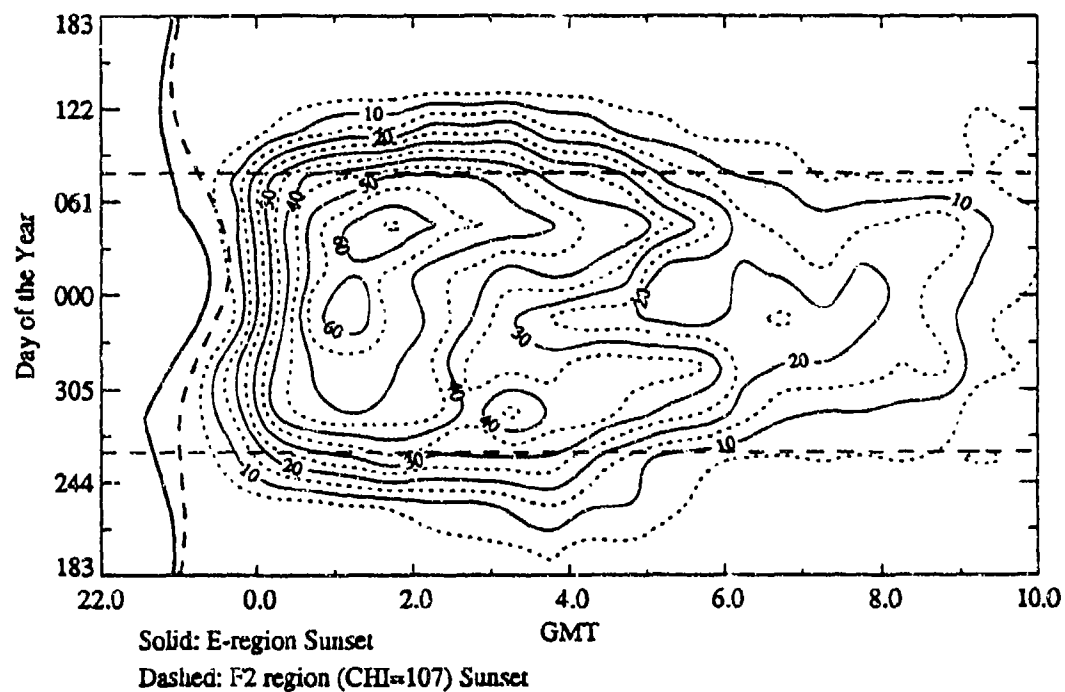
Appendix B. Data Plots — Variation with Geomagnetic Activity (K_p)

The figures in this appendix illustrate how the diurnal/seasonal pattern of occurrence statistics ($S_4 > 0.5$) varies as a function of geomagnetic activity level (as specified by K_p at the time of observation) at Huancayo (VHF), Manila (VHF), and Ascension Island (L-band). There are four plots for each station, one for each of four ranges of K_p : All K_p , $K_p \leq 20$, $20 < SSN \leq 40$, and $K_p > 40$. The bin size in all plots is 30 minutes in GMT by 30.5 days (one month) in day of the year.

The heavy solid line on each plot shows the variation of the time at which both E-region ends of the IPP field line with day of the year, and the heavy dashed line shows the variation of the time at which F2-layer sunset occurs (defined as $\chi = 107^\circ$). The horizontal dashed lines indicate the equinoxes.



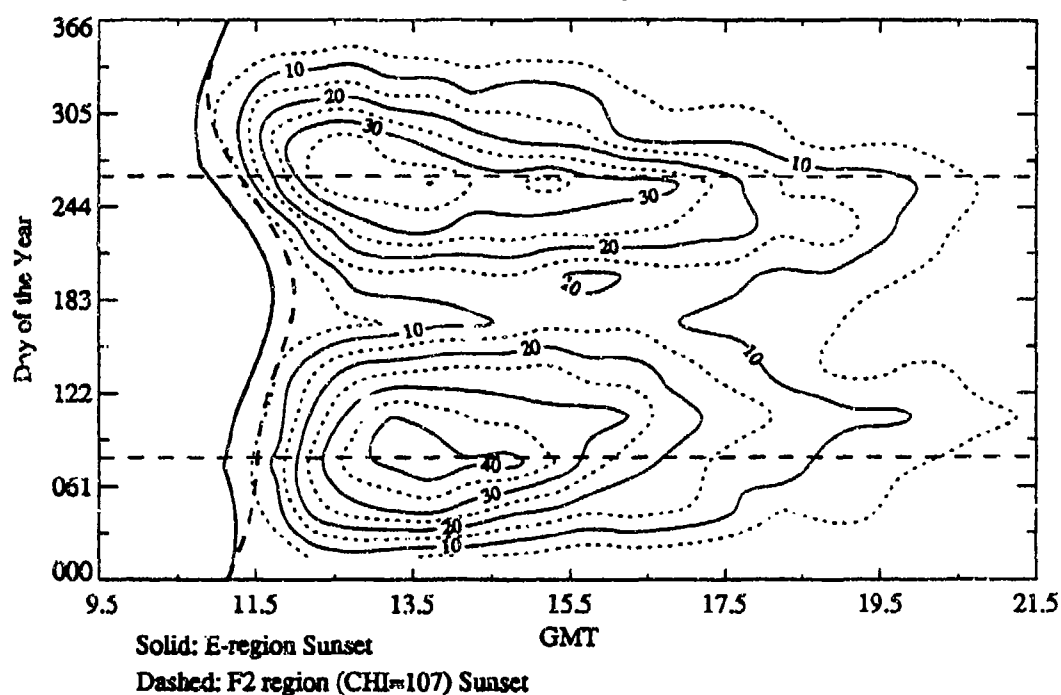
Huancayo-MARISAT (VHF)



All SSN
20 < Kp <= 40
Total Points: 52,480
Points > 0.5: 7,699

Manila-FLEETSAT (VHF)

Percent of Time S4 > 0.5



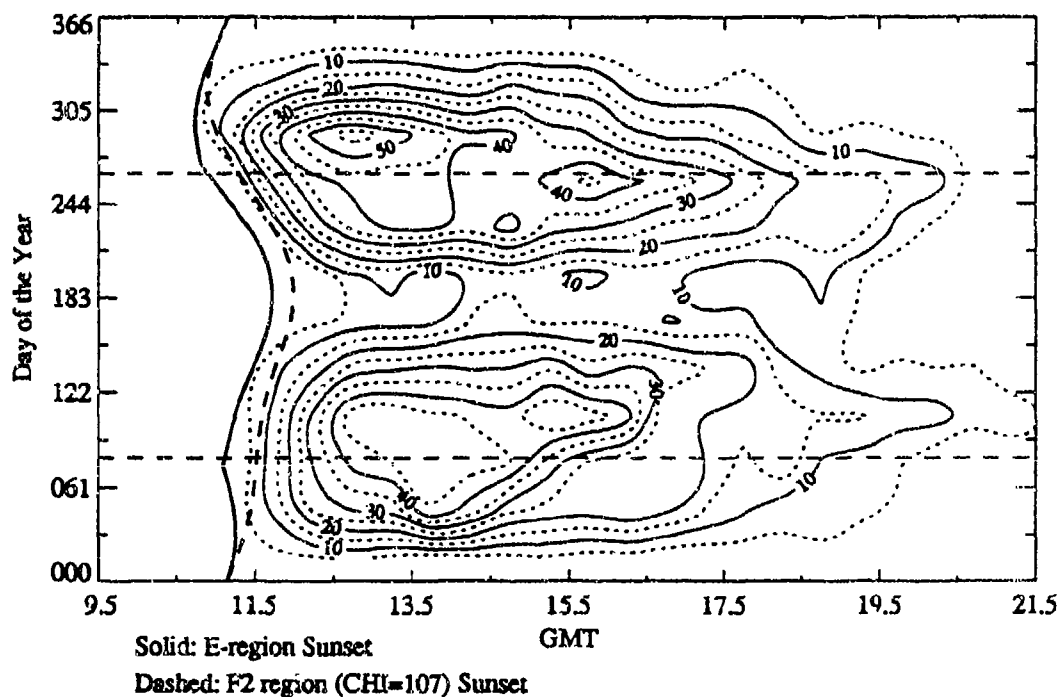
All SSN

All Kp

Total Points: 80,155

Points > 0.5: 8,210

Percent of Time S4 > 0.5



All SSN

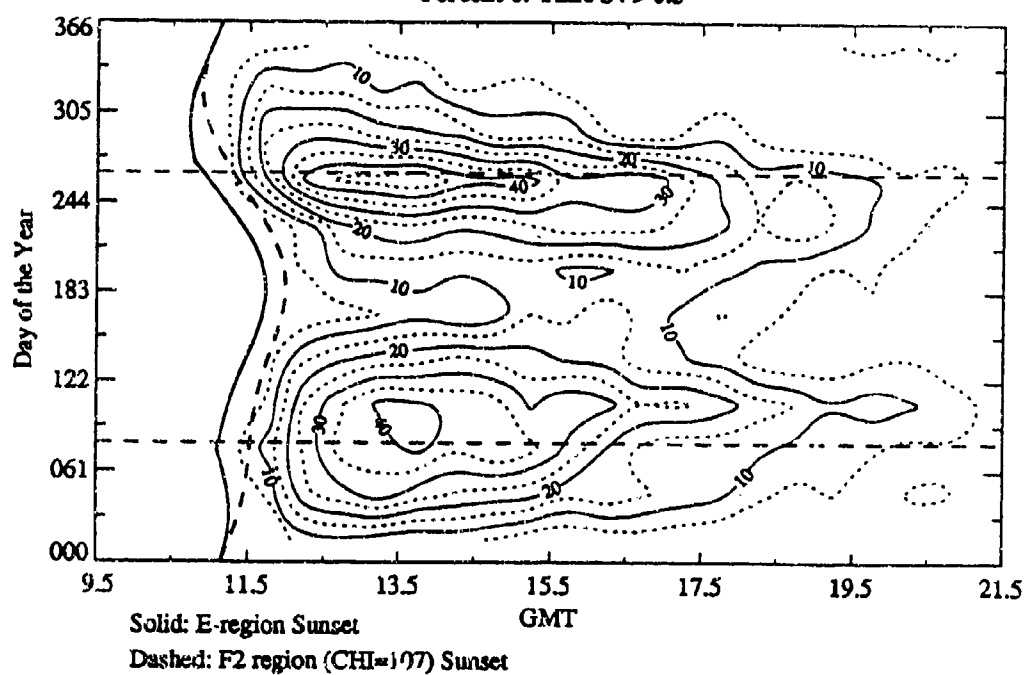
Kp <= 20

Total Points: 28,621

Points > 0.5: 3,335

Manila-FLEETSAT (VHF)

Percent of Time $S4 > 0.5$



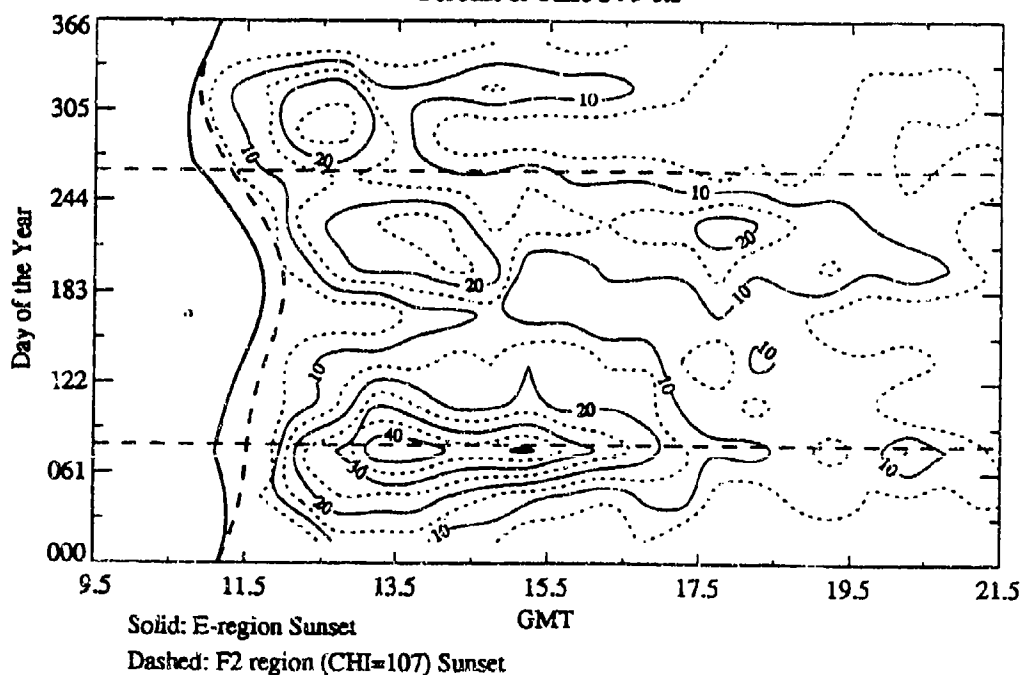
All SSN

$20 < Kp \leq 40$

Total Points: 38,145

Points > 0.5 : 3,758

Percent of Time $S4 > 0.5$



All SSN

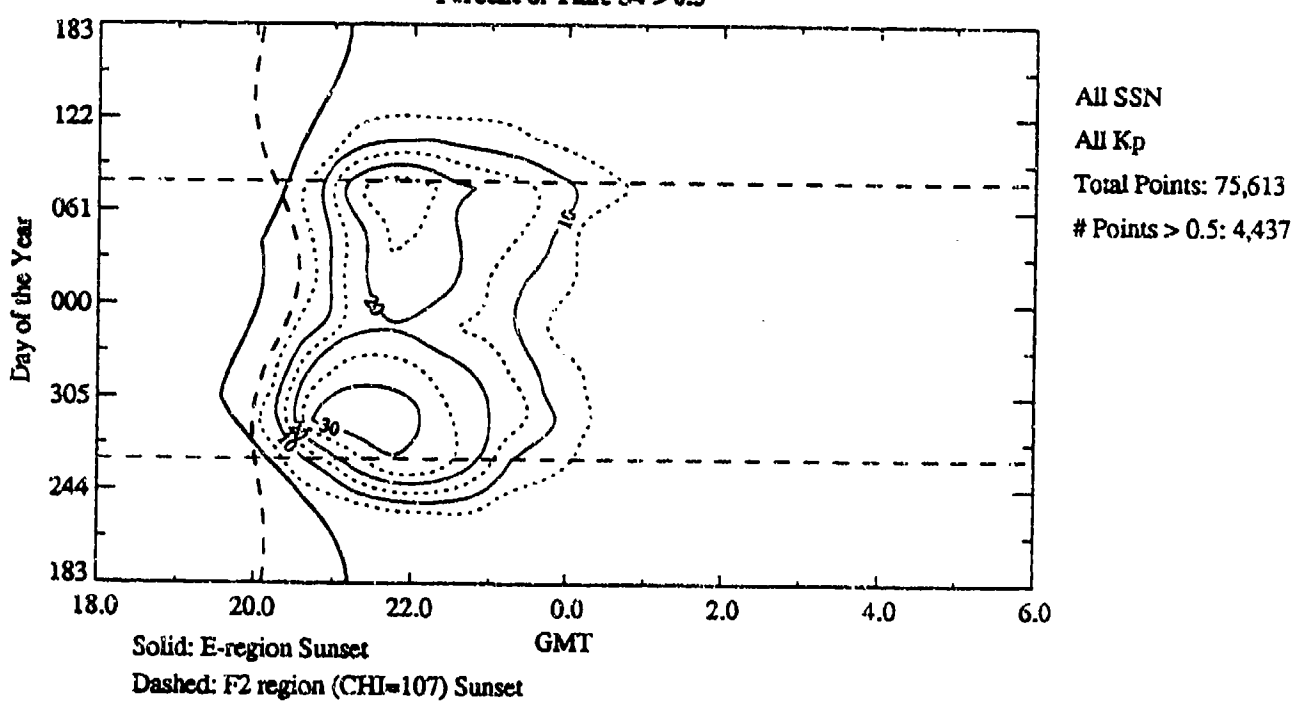
$Kp > 40$

Total Points: 13,389

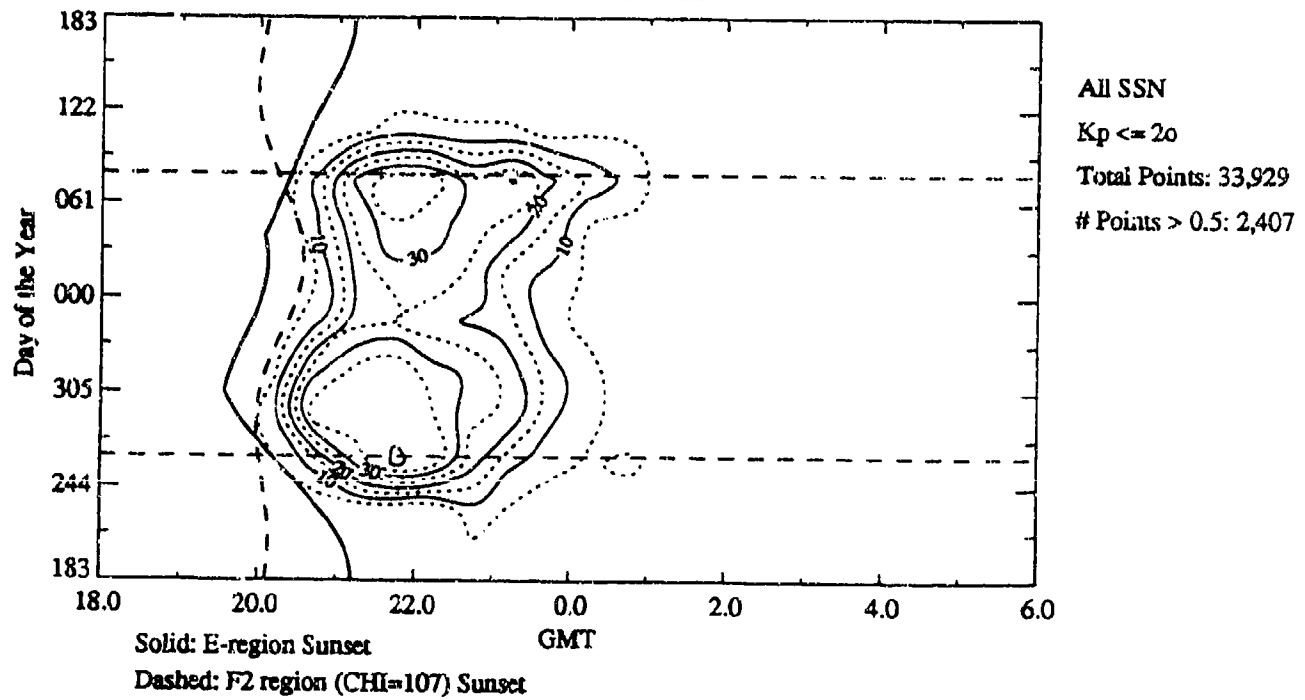
Points > 0.5 : 1,117

Ascension Is.-MARISAT (L-band)

Percent of Time S4 > 0.5

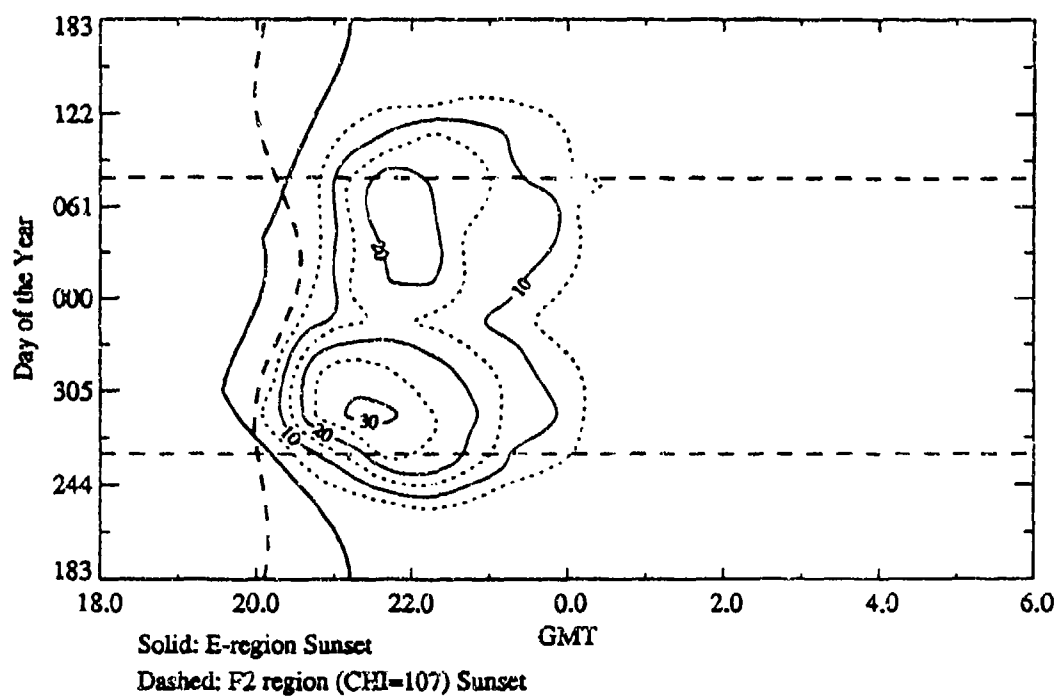


Percent of Time S4 > 0.5

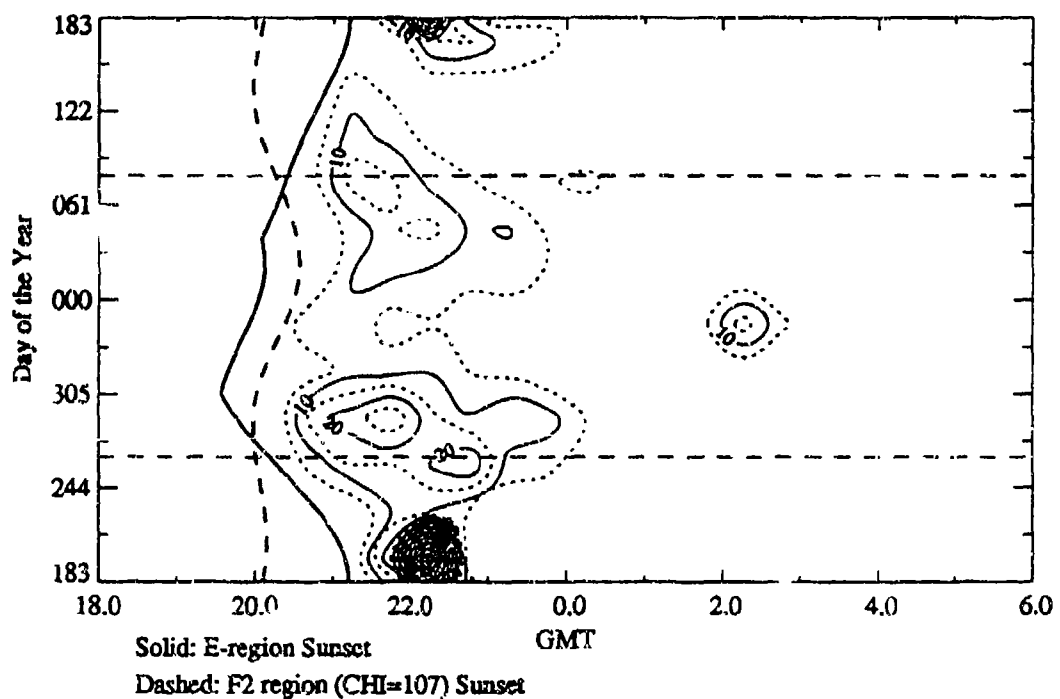


Ascension Is.-MARISAT (L-band)

Percent of Time $S4 > 0.5$



Percent of Time $S4 > 0.5$



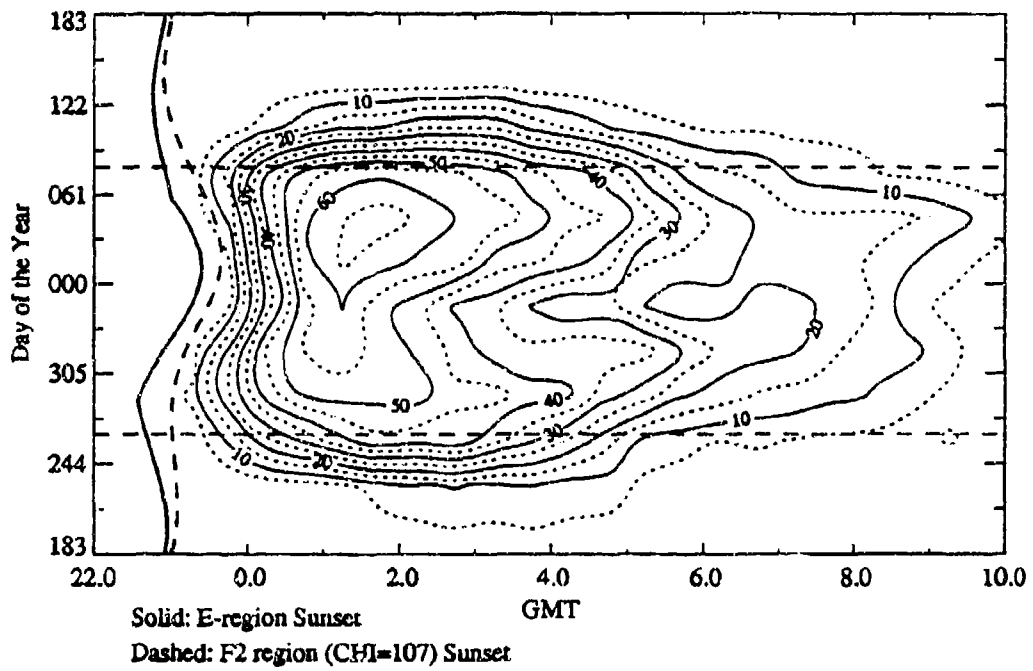
THIS PAGE INTENTIONALLY LEFT BLANK

Appendix C. Data Plots -- Variation with Geomagnetic Activity (K_{pSS})

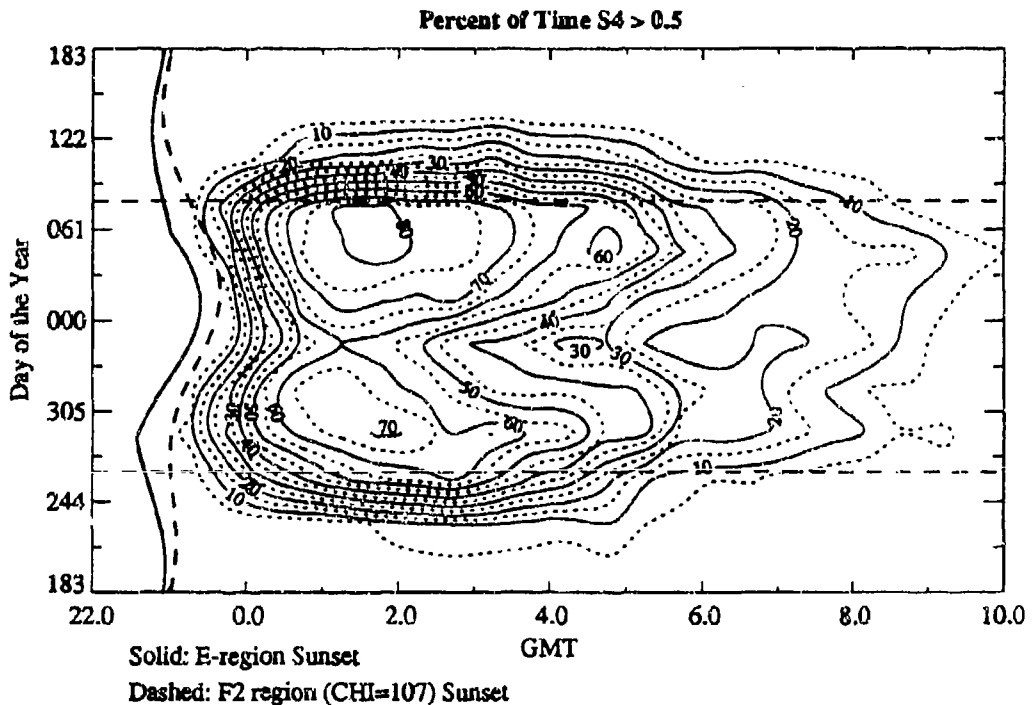
The figures in this appendix illustrate how the diurnal/seasonal pattern of occurrence statistics ($S_4 > 0.5$) varies as a function of geomagnetic activity level (as specified by K_p at the time of local sunset) at Huancayo (VHF), Manila (VHF), and Ascension Island (L-band). There are four plots for each station, one for each of four ranges of K_{pSS} : All K_{pSS} , $K_{pSS} \leq 2^\circ$, $2^\circ < SSN \leq 4^\circ$, and $K_{pSS} > 4^\circ$. The bin size in all plots is 30 minutes in GMT by 30.5 days (one month) in day of the year.

The heavy solid line on each plot shows the variation of the time at which both E-region ends of the IPP field line with day of the year, and the heavy dashed line shows the variation of the time at which F2-layer sunset occurs (defined as $\chi = 107^\circ$). The horizontal dashed lines indicate the equinoxes.

Huancayo-MARISAT (VHF)
 Percent of Time $S4 > 0.5$



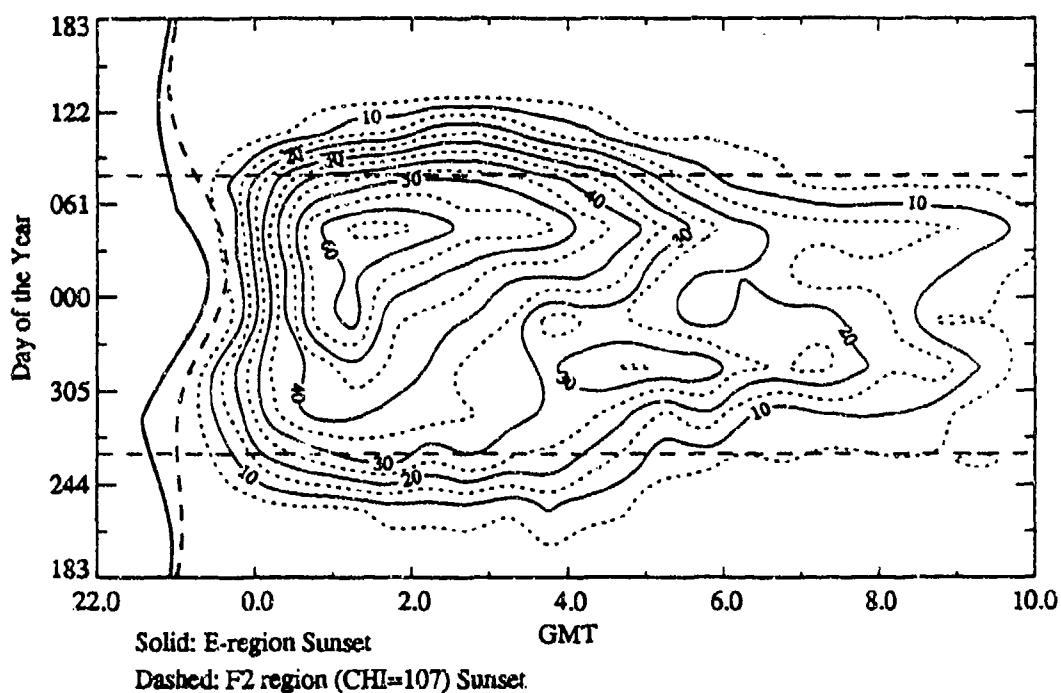
All SSN
 All Kp(SS)
 Total Points: 124,474
 # Points > 0.5: 18,654



All SSN
 Kp(SS) ≤ 2.0
 Total Points: 56,746
 # Points > 0.5: 9,995

Huancayo-MARISAT (VHF)

Percent of Time S4 > 0.5

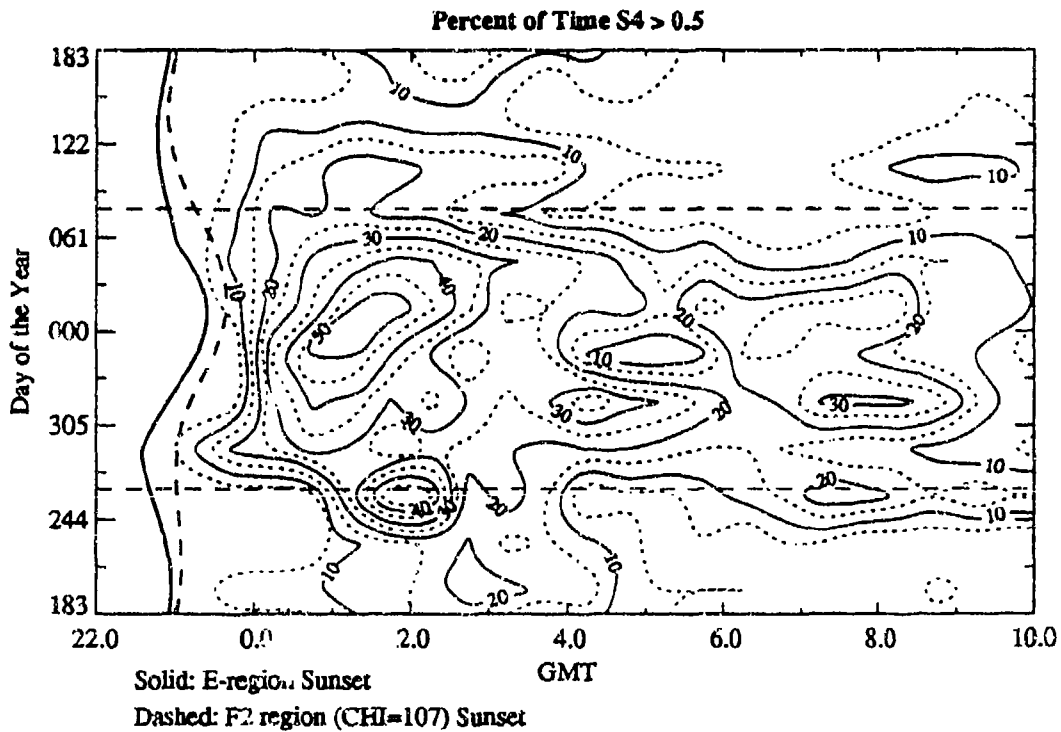


All SSN

$$2c < K_p(SS) \leq 40$$

Total Points: 51,679

Points > 0.5: 6,813



All SSN

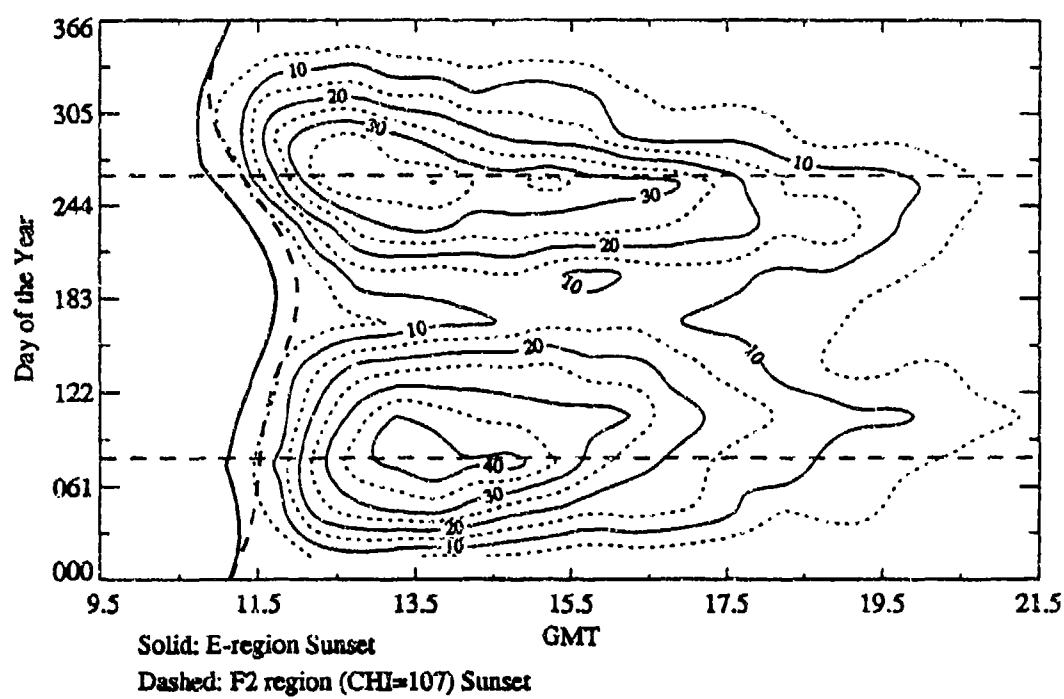
$$K_D(SS) > 40$$

Total Points: 16,049

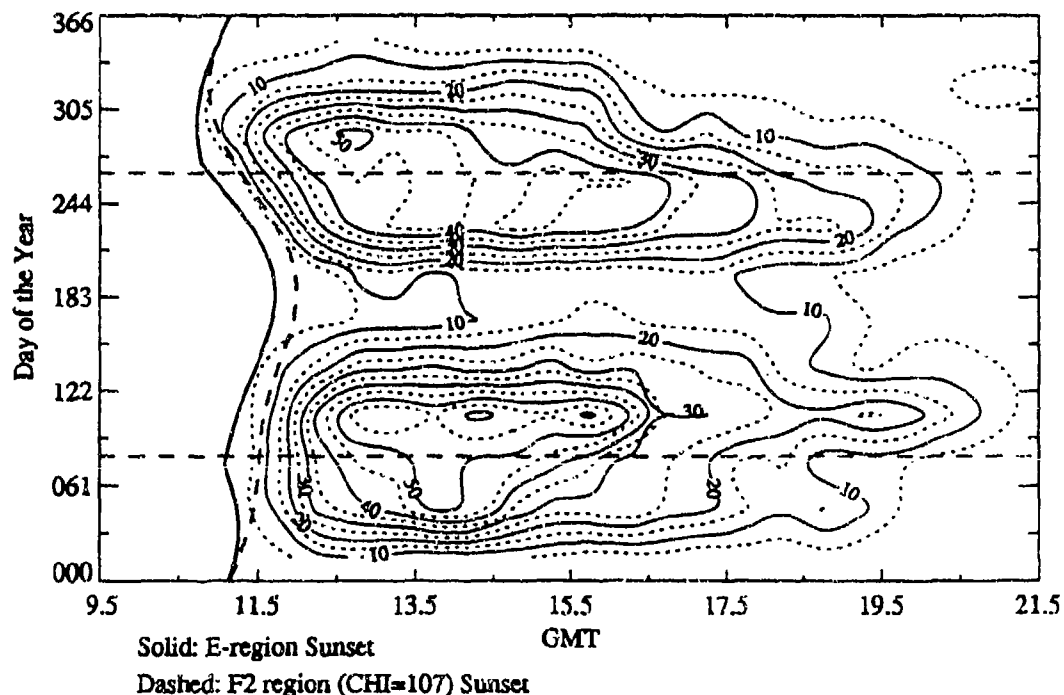
Points > 0.5: 1.846

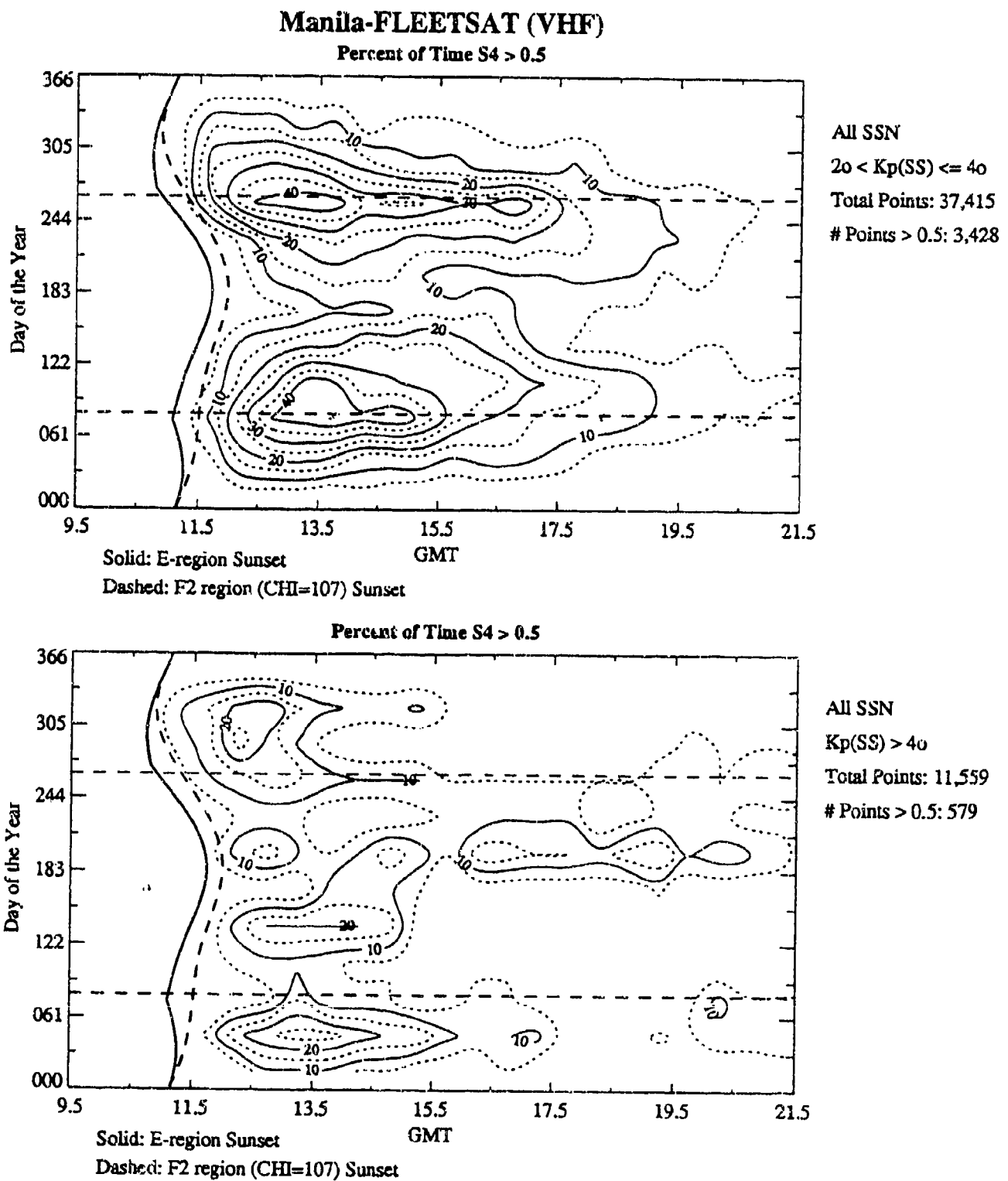
Manila-FLEETSAT (VHF)

Percent of Time $S4 > 0.5$



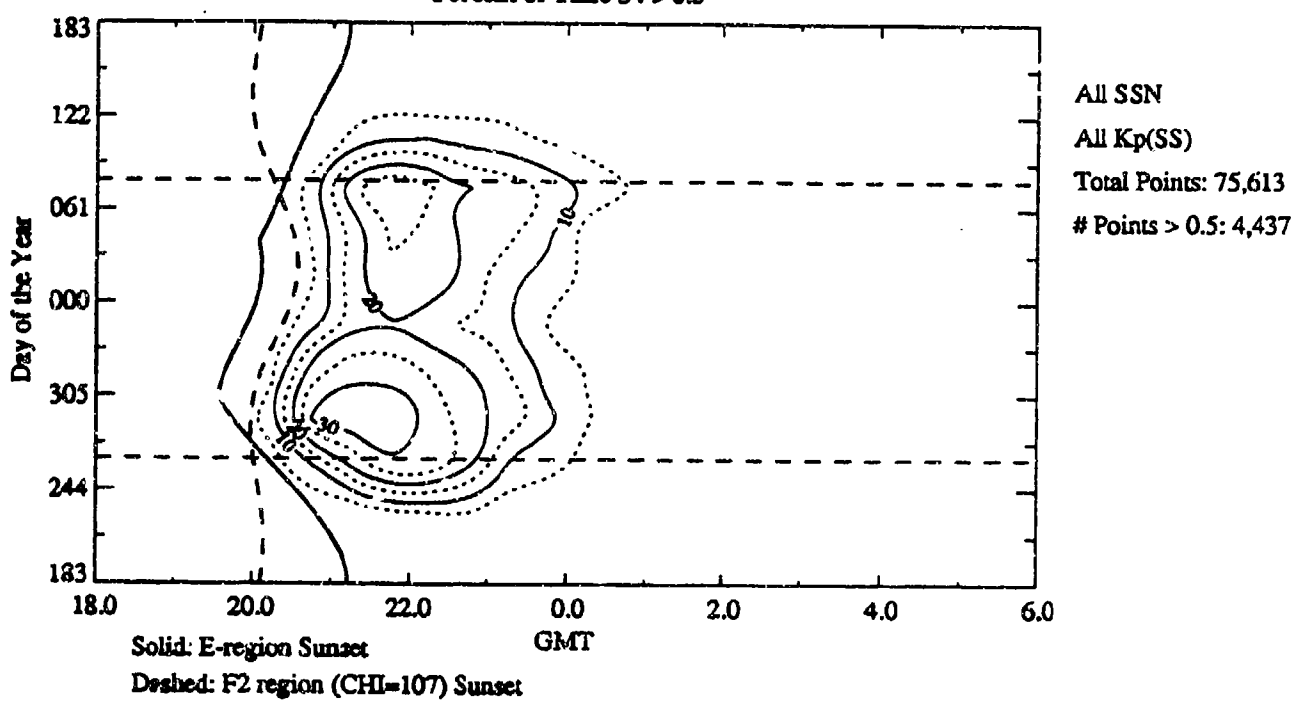
Percent of Time $S4 > 0.5$



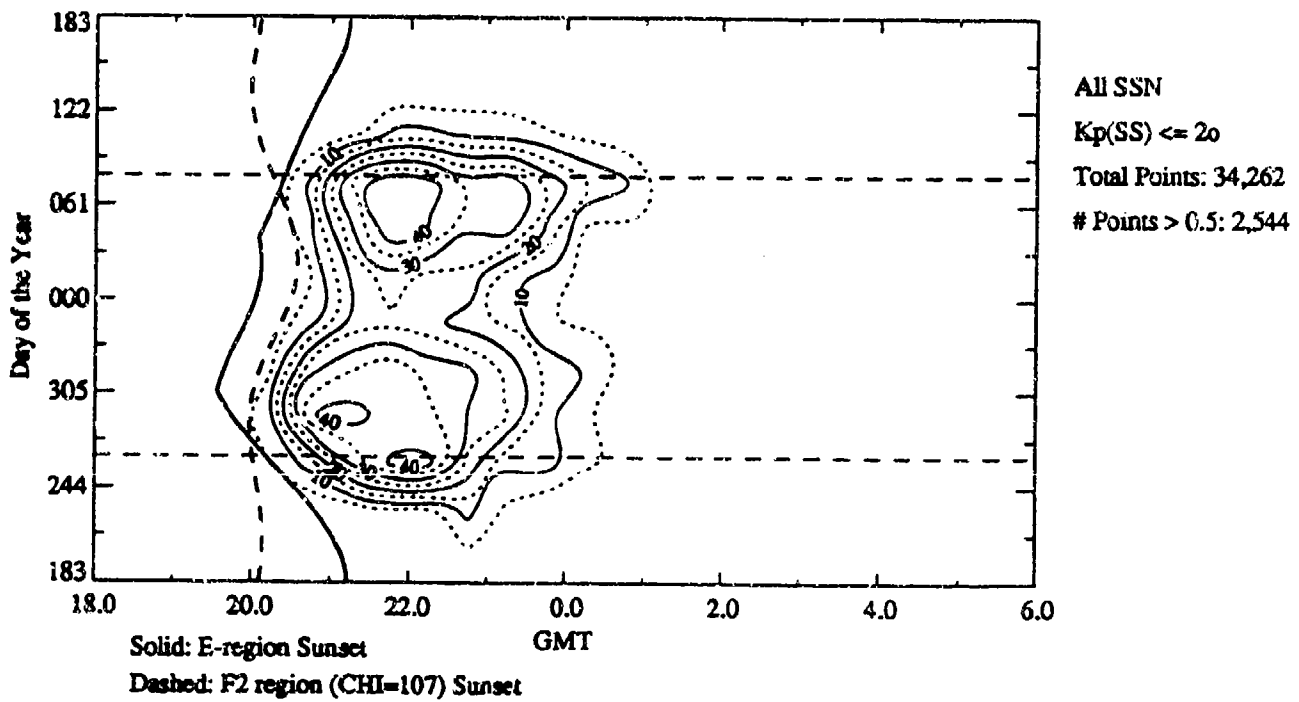


Ascension Is.-MARISAT (L-band)

Percent of Time $S4 > 0.5$



Percent of Time $S4 > 0.5$



Ascension Is.-MARiSAT (L-band)

Percent of Time $S4 > 0.5$

